THE INFLUENCE OF SURFACE CURVATURE ON POLYMER BEHAVIOR AT INORGANIC SURFACES

A Thesis
Presented to
The Academic Faculty

by

Grady A. Nunnery

In Partial Fulfillment
of the Requirements for the Degree
Doctor of Philosophy

School of Materials Science and Engineering
Georgia Institute of Technology
May 2010

THE INFLUENCE OF SURFACE CURVATURE ON POLYMER BEHAVIOR AT INORGANIC SURFACES

Approved by:

Professor Rina Tannenbaum
School of Materials Science and Engineering
Georgia Institute of Technology, Advisor

Professor Karl Jacob
School of Polymer, Textile and Fiber Engineering
Georgia Institute of Technology

Professor Hamid Garmestani
School of Materials Science and Engineering
Georgia Institute of Technology

Professor Preet M. Singh
School of Materials Science and Engineering
Georgia Institute of Technology

Professor Gleb Yushin
School of Materials Science and Engineering
Georgia Institute of Technology

Date Approved: 4 April 2009

To “The smith also sitting by the anvil, and considering the iron work, the vapour of the fire wasteth his flesh, and he fighteth with the heat of the furnace: the noise of the hammer and the anvil is ever in his ears, and his eyes look still upon the pattern of the thing that he maketh; he setteth his mind to finish his work, and watcheth to polish it perfectly:”

Ecclesiasticus 38:28

ACKNOWLEDGEMENTS

I would like to thank Prof. Rina Tannenbaum, my primary advisor, and Prof. Karl Jacob, my coadvisor, as well as the other members of my Ph.D. committee: Professors Hamid Garmestani, Preet Singh, and Gleb Yushin.

Many of my group members also deserve my praise: Dr. Erin Camponeschi Brotherson, who was always eager to help; Dr. Melissa Zubris Williams and Dr. Kasi David, whose work heavily influenced mine; and other group members, among them Dr. Jeremy Walker, Dr. Cantwell Carson, Dr. Lawrence Pranger, Rolando Gittens, Il Tae Kim, and Jung Hwa Park.

Other colleagues who have been particularly helpful include: Dr. Charles Capozzi, Dr. Lionel Vargas, Dr. Melanie Kirkham, Ryan Adams, Matthew Kincer, Lisa Linhardt, David Safranski, and Kathryn Smith.

Many faculty and staff have also been extremely helpful: Prof. Thomas Sanders, Prof. Naresh Thadhani, Prof. Allen Tannenbaum, Dr. Eli Hershkovitz, Susan Bowman, Dr. Jung-Il Hong, Dr. Mike Haluska, Prof. Jason Nadler, Prof. Kyriaki Kalaitzidou, Dr. Lisa Rosenstein, Prof. Rosario Gerhardt, Dr. Yolande Berta, Dr. Yong Ding, and the good people at the Georgia Tech Library in general and its interlibrary loan office in particular.

I would also like to acknowledge the kindness and assistance of the students, faculty, and staff of Technion–Israel Institute of Technology, especially: Neta Shomrat, Ilia Platzmann, Prof. Yachin Cohen, and Dr. Rafail Khalfin.

I would also like to thank the Institute for Paper Science and Engineering at the Georgia Institute of Technology, specifically Prof. Sujit Banerjee, Prof. Tim Patterson, Dr. Roman Popil, Prof. Ronald Rousseau, and Prof. Norman Marsolan for their promotion of a healthy environment for learning and for support of this research.

TABLE OF CONTENTS

LIST OF TABLES

LIST OF FIGURES

SUMMARY

Nanoscale surfaces were examined in order to determine the influence of surface curvature on polymer behavior at polymer-ceramic interfaces, as well as the influence of nanoparticles in cellulosic media.

Poly(methyl methacrylate) and block copolymers thereof were adsorbed onto porous alumina substrates of various pore sizes in order to determine how polymer and copolymer adsorption behavior at nanoscale surfaces differs from adsorption onto flat surfaces. It was determined that chain density on concave surfaces dramatically decreases as curvature increases in much the same way that it does on convex surfaces (e.g. on the surface of nanoparticles), and physical models are provided to explain this similarity. Diblock copolymer adsorption is observed to vary dramatically with solvent quality and block asymmetry and can be correlated with the surface curvature very similarly to the adsorptive behavior of homopolymers on those same surfaces.

The addition of nanoparticles to cellulosic media was investigated as a means to significantly modify the properties of cellulosic composites with minimal additions of nanoparticles. Although cellulose is among the most abundant polymers on earth, its primary uses are limited to bulk commodity goods, such as paper and textiles. This work demonstrates a simple means to control cellulosic fluid viscosity, thereby increasing the versatility of these biopolymers in additional applications with higher value-added potential. The formation of iron-cellulosic nanocomposites by the *in-situ* thermolysis of metal carbonyls to form metallic nanoparticles was performed and was analyzed by viscometry among other techniques. It was determined that the nanocomposites that were formed exhibited significantly increased viscosity, up to the point of gelation.

Additionally, an introduction to the expansive field of nanocomposites is provided, including how and why composite properties change abruptly as filler size approaches the nanoscale. An extensive background on this diverse field as it relates to the current work is provided with an emphasis on cellulosic nanocomposites and the dependence of curvature on polymer-surface interactions. A

detailed account of the experimental work relevant to this work is provided, including materials and characterization methods. Future work is proposed for both cellulosic nanocomposites as well as for curvature-dependent polymer adsorption. Finally, conclusions are drawn from the entire work and its implications to the greater field of nanocomposites.

CHAPTER I

INTRODUCTION

The properties of a material are often improved by additional phases. Among the many reasons to add filler to a matrix to form a composite are: mechanical property (*e.g.* stiffness, strength, toughness) improvement, thermal or electrical conductivity improvement, and control of coefficient of thermal expansion. [1] A decrease in filler size down to the nanoscale (< 100 nm) has two notable effects. The first, quantum confinement, is mentioned only for completeness and is not explored further in this text. The second, which will be the focus of this work, is the increase in specific surface area. Many composite properties are governed by interfacial interaction; therefore, nanocomposites—composites in which at least one dimension of one phase is smaller than 100 nm—are remarkable because of the high specific surface area of such nanoscale filler. [2]

It can be shown that the specific surface area of a sphere scales with $1/r$, r being the radius of the sphere. Therefore, halving the radius of a particulate filler will result in a doubling of its specific surface area. Let us now consider a one liter cube that is filled with 0.5236 volume percent spherical filler of radius r. It is obvious that the filler volume is .005236 m^3 or 523.6 cm^3, which would result in r = 5 cm. As radius decreases from this maximum, a dramatic increase in total surface area is observed, and this high surface area is one of the key characteristics of nanocomposites. This system is shown graphically in Figure 1.1.

One of the more well-known examples of nanoscale filler and how it improves composite properties is a composite in which nanoscale-thick platelets of montmorillonite clay are dispersed within a nylon matrix. Nylon 6-montmorillonite nanocomposites show significant increases over bulk nylon in tensile and flexural moduli, tensile and flexural strength, and heat distortion temperature with only a few weight percent of filler. [3] Such a small amount of filler imparts such significant changes in properties because of the nanoscale features of montmorillonite. In the region around a clay platelet (up to about 100 nm away from the surface), the nylon adopts a conformation that is much more ordered than bulk nylon 6. This increased crystallinity leads to the phenomena listed

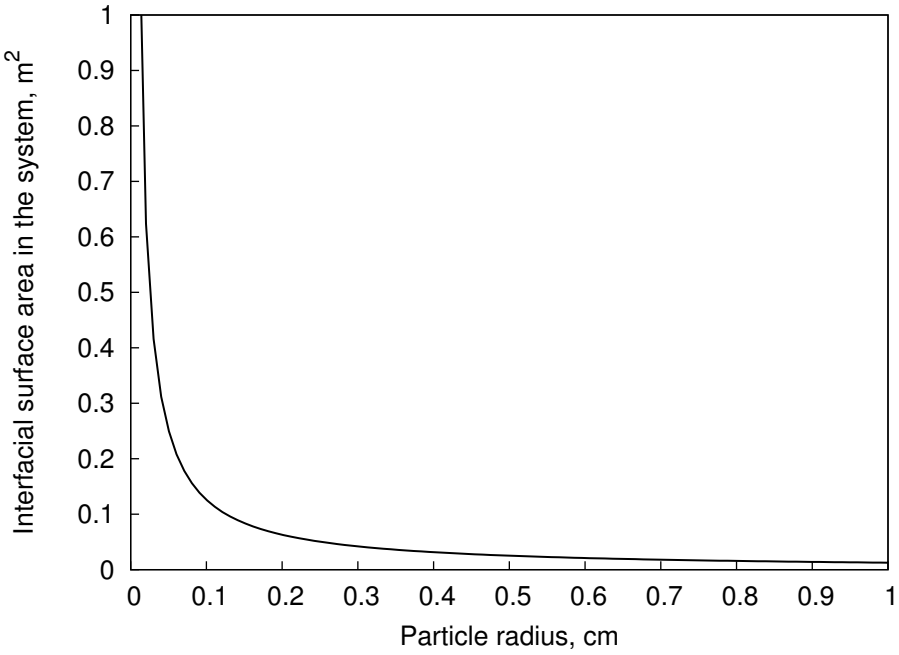

Figure 1.1: Interfacial surface area in the described composite system *vs.* particle radius.

above. [4] It is easy to see that large macroparticles with identical chemical surfaces as montmorillonite (such as micron-sized aluminosilicate crystals) would not affect as much polymeric volume as 50 nm thick clay platelets would. Because of the large specific surface area of nanoscale filler (see Figure 1.1), a large volume of polymer is constrained. It is unsurprising, then, to learn that a mere 5 weight percent of montmorillonite can nearly double the percent crystallinity of nylon 6 from approximately 35% to approximately 70%. [3]

Many properties change as matter becomes smaller and smaller. X-ray diffraction peaks broaden, and semiconductor band gaps increase. In order for these phenomena to be observed, the particles must be quite small–much, much smaller than one micron. A metal's melting point is known to decrease as grain size decreases. This is not because of a violation of the laws of thermodynamics. Rather, the metal surface, which is more disordered and therefore requires less energy to melt, occupies a huge fraction of the total volume. [5] This particular property–the change in melting point–is not a bulk property at all but rather a surface property. Surface effects are critical to comprehension of nanoparticle and nanocomposite properties.

This thesis is a discourse on nanoscale surfaces much like the examples above and *how and why they influence the properties of composites that contain them*. The general questions to be answered

in this dissertation are: 1) How much nanoscale filler is required to induce significant property effects? and 2) How and at what point do curved surfaces begin to behave fundamentally differently than flat surfaces? But before those questions are addressed, some background information on nanocomposites and their properties is in order.

CHAPTER II

BACKGROUND

2.1 Chapter Overview

This chapter will provide critical background information regarding the primary topics of this thesis: nanocomposites in general and cellulosic nanocomposites in particular. Major topics include: general nanocomposite synthesis, nanocomposite synthesis *via* metal carbonyl decomposition, cellulose and cellulosic nanocomposites, polymer adsorption to curved surfaces, and anodic aluminum oxide as a concave substrate.

2.2 Nanocomposites and Their Synthesis

As previously mentioned, a nanocomposite is a multiphase solid system with at least one phase in the size range of 1-100 nm, and many methods exist for nanocomposite synthesis. Common synthetic routes are provided as Table 2.2, which is presented to be neither exhaustive nor exclusive but rather exemplary. Four broad categories are presented: simple admixture, complex admixture, *in situ* polymerization among nanoparticles, and *in situ* nanoparticle formation among polymers.

Perhaps the simplest nanocomposite synthesis method is the admixture of nanoparticles into a polymer melt, followed by cooling. An example is the extrusion of a mixture of silver nanoparticles and melted polypropylene. [6] Additionally, admixture may occur in a more complex system, such

Table 2.1: Common Nanocomposite Synthesis Methods and Examples

Method	example
Simple admixture	Twin-screw extrusion of polypropylene and silver nanoparticle powder [6]
Complex admixture	Regeneration of cellulose from a mixture that includes titania nanoparticles [7]
In situ polymerization	Synthesis of nylon among clay platelets [8, 9]
In situ nanoparticle synthesis	Precipitation of metal nanoparticles from salts on fibers [10]

as a polymer solution. For example, Zhou *et al.* formed nanocomposites by mixing nanoscale titania into a cellulosic solution before regeneration of a cellophane film. While the modified cellulose was dissolved, nanoparticles were added to the system. [7] One disadvantage of the admixture methods is aggregation, which occurs often in these systems. [11]

Yet another method of nanocomposite synthesis is polymerization among nanoparticles. The classical example of this method is the polymerization of nylon-6 from ϵ-caprolactam among montmorillonite platelets and has been mentioned in Chapter 1. [8,9]. The present author had the pleasure of working with Drs. L. Pranger and R. Tannenbaum on a similar system (poly(furfuryl alcohol)-clay nanocomposites) in addition to the work discussed in the current document. [12]

Not only can polymers be synthesized among nanoparticles, but also nanoparticles can be synthesized among polymer chains, and this *in situ* method will be discussed intensively in the current work. An example of this method is the precipitation of metals from metal salts within polymeric media. Some of the earliest known polymeric nanocomposites were formed through this method well before Carothers first synthesized nylon. During the early 20th century, cellulose and cellulose acetate fibers were impregnated with silver or gold salts, which were then reduced to form zero-valent nanoparticles [11]. More recent research, with the aid of electron microscopy, has elucidated this method and shown that it results in particle formation within fiber voids [13] and on fiber surfaces. [10]

Also, inorganic particles can be formed *in situ* in polymer *solutions* (as opposed to bulk solids or melts) in order to form nanocomposites. For example, Paul *et al.* precipitated polysaccharide-coated iron oxide particles from iron salts which were in solution with branched low molecular weight polysaccharides and OH^-. [14] Again, Table 2.2 is not meant to be exclusive or exhaustive. In fact, it most assuredly is not. For example, prior to regeneration of cellulose, inorganic particles can be formed *in-situ* in a polymer solution, thereby combining pathways two and four as presented in the table. [15]

A notable *in situ* nanocomposite formation method is the thermolysis or hydrolysis of metal-containing precursors in polymeric media. This category includes metal carbonyl decomposition in films [16] as well as the hydrolysis of metal alkoxides in solutions. [17] Both of these methods yield narrow size distributions. The thermolysis of metal carbonyls for nanocomposite synthesis will be a

major focus of this thesis, and, as such, it will be discussed in greater detail in the following section.

2.3 Nanocomposite Formation via Metal Carbonyl Decomposition

Nanocomposite formation from the thermal decomposition of metal carbonyls in polymeric systems has a rich history dating back to the mid 20th century, when Hess and Parker [18] and Thomas [19] nearly simultaneously reported the synthesis of colloidal cobalt nanoparticles in macromolecular media *via* this method. Among the key observations they made regarding particle size were: 1) Particle diameter is generally small, with most syntheses resulting in average diameters < 100 nm; 2) Size distribution is quite narrow, with 85% of all particles within a factor of two of the mean diameter; and 3) Polymers with polar moieties disperse the resultant clusters better than those with nonpolar moieties. These observations have been supported by decades of research for nanoparticles synthesized by metal carbonyl thermolysis in polymeric media, and they are among the reasons that this method is so attractive as a pathway to nanocomposite synthesis. In fact, it is the current primary method of incorporating ferromagnetic nanoparticles into polymers. [11]

Thomas [19] suggested that not only cobalt but also nickel and iron carbonyls would yield nanoparticles in a similar way in polymeric media. Griffiths *et al.* [20] and Smith and Wychick [21] verified this in 1979 and 1980, respectively, and confirmed similar trends for iron and nickel as those observed for cobalt.

Though the mechanism of metal carbonyl thermal decomposition is complex, the overall reaction is quite simple, shown for iron pentacarbonyl below:

$$\mathrm{Fe(CO)_5} \rightleftharpoons \mathrm{Fe} + 5\mathrm{CO_g} \tag{2.1}$$

The above simplification omits the numerous (and highly reactive) intermediates, such as ions, radicals, and unsaturated metal complexes. The actual mechanism consists of discrete losses of CO ligands to form unstable intermediates, which can recombine with CO gas or join with other partially decomposed molecules to form clusters. The latter is favored at low relative CO pressure [22]. A more accurate depiction is the following:

$$\mathrm{Fe(CO)_5} \rightleftharpoons \mathrm{Fe(CO)_m} + (5-\mathrm{m})\mathrm{CO_g} \rightleftharpoons \mathrm{Fe_s} + 5\mathrm{CO_g} \tag{2.2}$$

The above equation is not meant to describe the entire process, which may include ions and radicals. Furthermore, it is insufficient to describe cluster growth, aggregation and dissociation. Nonetheless, it demonstrates the overall reaction quite well.

The resultant zero-valent metal can react with other chemical species to form compounds such as FeOOH, Fe_2O_3, Fe_3O_4, and Fe_3C [11]. It is important to note that the exclusion of impurities and oxidants from the system can severely limit these side reactions. In fact, zero-valent iron can be formed in clean, inert conditions. These zero-valent particles are stable when exposed to oxygen, due to a passive oxide layer (γ Fe_2O_3) approximately 30 Å thick. [20]

The kinetics of decomposition are complex, and the order of the overall reaction is not agreed upon (*n.b.* the kinetics observed experimentally in the current work are first order with respect to organometallic precursor concentration). However, decompositions in polymeric systems have led some researchers to conclude that the clustering process is governed by nucleation and growth kinetics. Dan *et al.* proposed that nucleation-dominated kinetics could yield the narrow distributions that are commonly observed. [23]

Manipulation of the decomposition media affects the resultant nanoclusters. For example, carbonyl decomposition in inert atmospheres yields zero-valent metallic particles almost exclusively, while the presence of an oxidizing agent—even a weak one—yields metal oxides. [22] It should come as no surprise, therefore, that the presence of polymer chains can have profound effects on the nanoparticle synthesis.

2.4 The Effect of Polymeric Media in Nanoparticle Synthesis via Metal Carbonyl Thermolysis

The products of metal carbonyl decomposition change when polymers are added to the system. [23, 24] For example, decomposition in polystyrene (PS) melt has been shown to differ significantly from decomposition in toluene, although the two systems feature similar chemical structures. The difference is that PS benzyl moieties are chemically bound to a hydrocarbon backbone, whereas toluene molecules are unconnected. The difference in the resultant nanocluster size and size distribution is striking (Table 2.4). [25]

Particles synthesized in PS were much smaller than those synthesized in pure toluene. Also,

the size distributions were quite narrow—again a general feature of most particles synthesized by metal carbonyl thermolysis in polymeric systems. [26] Furthermore, decompositions in polymer solutions have been shown to differ significantly from decompositions in polymer melts. The size of the resultant particles synthesized in a melt does not depend upon molecular weight; however, molecular weight does affect the size of particles obtained from decomposition in solution. [23]

In addition to clustering, the previously mentioned reactive intermediates that develop during the decomposition process can react and interact with polymer chains, leading to particle attachment, polymer degradation, and cross-linking. [22] Among these, attachment is the most important because effective adsorption of a polymer layer onto a particle can prevent further cluster growth and flocculation and thus stabilize the particles. Forming and maintaining small particle sizes is crucial for many of the applications of such particles because an increase in size leads to a loss in specific surface area and, therefore, a sacrifice in available surface area for reaction and catalysis.

Metal carbonyl thermal decomposition in polymeric solutions yields nanocomposites. However, this simple one-step approach, which allows for the control of particle size, the prevention of flocculation, narrow size distributions, and the stabilization of particles due to polymeric influence, [27] has yet to be tested extensively for cellulosic nanocomposites. In order to discover the relationships between cellulose chemistry and synthesized particles, this research will investigate metal carbonyl decomposition in cellulosic systems.

2.5 Cellulose

While metal carbonyl decompositions have been conducted in a variety of polymeric solutions and melts, only a few have been conducted in cellulosic systems. In a 1959 patent, Schölzel proposed the thermal decomposition of $Fe(CO)_5$ vapor in heated cellulosic (and other polymeric) films in

Table 2.2: Comparison of Nanocluster Size and Size Distribution

System	Size(nm)
PS melt, M_W=250000 g/mol	67.2 ± 4.7
toluene	270 ±100

order to obtain a ferromagnetic coating for data storage. [28] Later, Shim and coworkers formed nanocomposites by decomposing iron carbonyls that were impregnated in cellulose acetate (CA) films. Such a technique is attractive because a cosolvent for both CA and iron carbonyls exists and because the films may easily be examined with infrared spectroscopy. [16]

Cellulose—a renewable polymer which accounts for over half of the carbon in the biosphere [29]—is primarily used for bulk, inexpensive products like paper and textiles. Although these industries obtain almost all their cellulose from trees or from cotton, this abundant biopolymer can be found in all other plants and even one animal—the tunicate. [30] Cellulose is a linear polysaccharide of D-glucopyranose units with beta 1-4 linkages, seen in Figure 2.1. The degree of polymerization varies from the hundreds (about 10^4 g/mol) for regenerated fibers (rayon and lyocell) to tens of thousands (about 10^6 g/mol) for some native cellulosic fibers. [31]

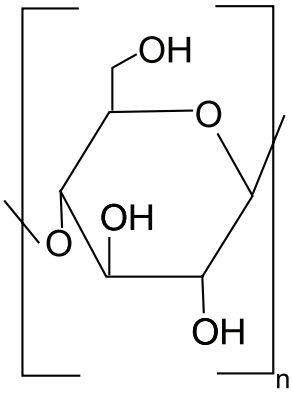

Figure 2.1: One repeat unit of cellulose

Figure 2.1, though an acceptable representation of cellulose's chemical structure, does not show the actual conformation of the chain, which is not planar but rather bent like a chair, which allows for much intrachain and interchain hydrogen bonding, providing strength to cellulosic materials. Furthermore, due to the β glycosidic bond, adjacent repeat units are inverted. [31]

Cellulose morphology is quite complex, with at least seven different polymorphs. Native crystalline cellulose exists as cellulose I (α or β). However, after regeneration (dissolving then precipitating) or mercerization (swelling with then removing OH^-), cellulose recrystallizes in a different form: cellulose II. Further treatment of either cellulose I or II with some amines yields cellulose III (III_I or III_{II}), which can be heated to obtain cellulose IV (IV_I or IV_{II}). [32]

Natural cellulose is never completely crystalline; much of the polymer is amorphous. Amorphous regions exist at microfibril surfaces, where the slightly curved chains feature a preferred orientation. As such, cellulose featuring tiny microfibrils (*e.g.* bacterial cellulose) is more amorphous than cellulose with larger microfibrils. Cellulose's alcohol groups (each repeat unit has three) contribute significantly to its structure and properties. In fact, one marked difference among the polymorphs is their different mechanisms of hydrogen bonding. Furthermore, the alcohol groups serve as common chemical modification sites. [32]

The modification of cellulose is not a new concept. Many alterations predate modern science. Modification for optical purposes (dyeing) has taken place for many millennia. [33] In the past two centuries, more elegant modifications, such as regeneration, esterification, and etherification, have arisen. For example, nitrocellulose—an ester derivative now used for DNA analysis—was discovered in the mid 19th century by Schönbein. Celluloid, the first known plastic—synthesized in 1868—was based upon cellulose, and rayon—regenerated cellulose fibers—was introduced in the early 20th century. [34]

Common cellulose chemical modification methods attack cellulose's many OH groups; each repeat unit features three—a primary group at C_6 and secondary alcohols at C_2 and C_3, which can be seen in Figure 2.2. The chemical modification of these hydroxy groups are limited only by the imaginations and capabilities of organic chemists. A common chemical modification scheme is etherification *via* nucleophilic substitution, illustrated below:

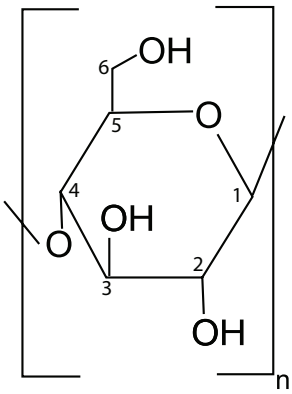

Figure 2.2: Cellulose carbon numbering scheme

$$\begin{aligned} \text{CellOH} + \text{OH}^- &\longrightarrow \text{CellO}^- + \text{H}_2\text{O} \\ \text{CellO}^- + \text{IR} &\longrightarrow \text{CellOR} + \text{I}^- \end{aligned}$$

where R is an organic group, such as CH_3 or C_6H_5.

Another chemical modification method is esterification. In general, esterification yields water-insoluble derivatives, as opposed to etherification, which generally yields water-soluble derivatives. Esterifcation is the reaction pathway to cellulose acetate (CA) synthesis:

$$\text{CellOH} + \text{CH}_3\text{COOH} \longrightarrow \text{CellOCOCH}_3 + \text{H}_2\text{O}$$

Note that the above reaction is favored in the presence of acid. CA, which can also be formed by treatment with acetic anhydride, is an industrially relevant derivative. Its early uses were primarily for coatings (*e.g.* for the exterior of airplanes), as textile fibers, and as films. More recent uses are cigarette filter tow [35] and scientific supplies such as filters and membranes.

Chemical modifications usually do not affect all of cellulose's alcohol groups, especially due to varying degrees of accessibility (due to crystallinity, for example). Furthermore, the C_2, C_3, and C_6 alcohols are not created equal. The C_2 hydroxyl group is the most acidic, so alkoxide ions are more likely to attack it, unless the substitution group is large. In that case, the C_6 alcohol—more removed from the main chain—is more reactive. [36]

Two parameters are necessary to describe the chemical alterations: molar substitution (MS) and degree of substitution (DS). DS is the average number of OH groups that have reacted per repeat unit; it varies from 0 to 3. MS, the average number of substituent molecules that have reacted per repeat unit, is necessary because further modification of many cellulose derivatives can occur not only on remaining unreacted hydroxyl groups but also on the recently added organic groups. [34]

Another method of cellulose modification is regeneration, in which the cellulose is solubilized (usually by a chemical modification) then reformed as fibers, films, or filaments of cellulose. One early regeneration method, the viscose process used to obtain rayon, involves ionization with base,

followed by treatment with CS_2 then treatment with acid to reform cellulose. A newer industrial regeneration method is dissolution in N-methylmorpholine-N-oxide followed by extrusion and washing. This process results in the formation of lyocell. Yet another method is precipitation from a cellulose-urea/thiourea solution. [34]

2.6 Adhesion, Adsorption, and Polymer Conformation at Surfaces

Of critical importance to composites—cellulosic or otherwise, nano or otherwise—is how the phases interact with each other at their interfaces. Felix and Gatenholm showed that a simple surface treatment of cellulose with a maleic anhydride-polypropylene copolymer greatly improves the mechanical properties of polypropylene(PP)-cellulose composites, causing a near doubling of breaking strength at some fiber loadings, as well as modest increases in bulk modulus. The primary reason attributed to these improvements is the improved interaction strength at the surface. The maleic acid groups along the copolymer chain interact strongly with the cellulosic surface, due to a chemical reaction. Unmodified PP-cellulose composites lack this specific, strong bonding and therefore show the markedly different mechanical properties described earlier. [37] Interfacial interactions strongly influence the properties of nanocomposites. Strong interactions between carbon nanotubes and their surrounding polymer matrix hinder crazing extension and reduce stress concentration, thereby making the composite tougher. [38, 39] Therefore, it is easy to see that any discourse on composites would greatly benefit from a discussion of polymer bonding at the surface. And regarding this particular topic, much has been written, and the remainder of this chapter will be devoted to polymer adsorption to surfaces and how it changes at the nanoscale.

Why would adsorption change at the nanoscale? Let us conduct a simple thought experiment. On a flat surface, one polymer chain bonds at a specific site on the surface. There is an energetic gain from this process because the polymer chain has some attraction to surface. However, it comes at a loss of conformational entropy because, due to the impenetrable surface and the anchor points, the chain has fewer available states. This adsorption of one chain has two noticeable effects on subsequent polymer chains that will adsorb: 1) the occupation of surface sites by the initially adsorbed polymer precludes additional polymer chains from those sites and 2) osmotic pressure prevents subsequent polymer chains from significantly penetrating the occupied volume *above* the surface. The

net effect is that in general, subsequent polymer chains must occupy different areas of the surface. Now imagine what happens when the flat surface bends, as in a nanoparticle. It is easy to see that a modestly low curvature would not significantly affect the way the polymer associates with the surface. However, as particle size decreases and curvature increases, the previously explained model breaks down. The energetic gain associated with adsorption remains the same, but the entropy loss is much, much greater for the nanoparticle. See, for example, Figure 2.3. This is the general problem addressed in a series of papers by Hershkovits *et al.*, who showed experimentally and theoretically that as the particle size decreases, the polymer makes fewer contact points, or anchors, with the surface both per chain and per unit surface area. [40–42] This model and its applicability to concave surfaces will be discussed in further detail in Chapter 4.

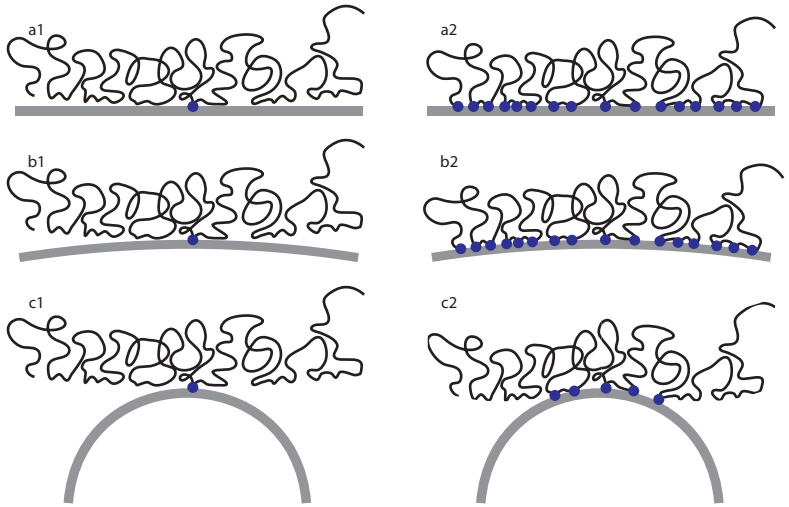

Figure 2.3: The general pictorial explanation of why polymer adsorption occurs differently on nanoscale surfaces than flat surfaces. In these three scenarios (a,b, and c), a polymer chain approaches the surface (left) and bonds to it in a particular manner (right). It is easy to see that slight bending (b) of a flat surface (a) will not significantly affect polymer adsorption. However, extreme bending of the surface (c) will significantly affect the entropic contribution, thereby influencing the manner in which the polymer associates with the surface.

2.7 Anodic Aluminum Oxide

Because much work has been reported regarding the convex alumina nanoparticle-PMMA system, [40–42] this work expands and develops that work in order to apply it to concave alumina. The particular concave substrate chosen for this particular work is anodic aluminum oxide, and the theory and practice of anodization will be described next.

Anodization of aluminum (and metals in general) has many applications in modern technology. The (only) traditional uses are protection of the bulk metal and surface modification. Anodic alumina films can be quite corrosion-resistant. Although the native oxide film, which is present on all aluminum, is protective, it is imperfect, due to its extreme thinness and due to electron transfer through the layer. However, this layer can be grown under anodizing conditions. And because the anodic oxide layer is thicker than the native oxide layer, it provides more electrical resistance. Such protection is necessary in corrosion-prone environments, such as seawater. Corrosion resistance is significantly improved, especially when the resultant pores are sealed. [43] In addition, because pigments and dyes absorb well to anodic alumina surfaces, presumably due to their high surface area, anodized aluminum oxide can be used in many circumstances for decorative purposes.

Other property changes are observed but are less significant than the protection and decorative versatility mentioned above. [44] However, the specific usage that will be discussed here in depth is the anodization of aluminum in order to form well-defined pores of various geometries, which are extremely relevant to nanotechnology. Before discussing this novel application of anodization, I will first discuss the theory and practice of anodizing aluminum in general.

The formation of a surface aluminum oxide film as a result of direct current applied to aluminum in an acidic electrolyte is known as anodizing. A simple diagram (Figure 2.4) shows the setup of a typical anodizing process. The aluminum, in acid solution, is connected to the positive terminal of a battery. Another metal, in this case lead, serves as the cathode and is connected to the negative terminal. The identity of the cathode is insignificant as long as it does not dissolve in the electrolyte.

It may be surprising that aluminum requires encouragement to oxidize, given the relative energetic favorability of Al^{3+} over aluminum. The half-reaction

$$Al^{3+} + 3\,e^- \rightleftharpoons Al_{(s)} \tag{2.3}$$

has a standard electrode potential ($E^o = -1.68$ V), which is much more negative than traditionally more corrosion-prone iron. The complete reaction

$$2\,Al + 3\,H_2O \rightleftharpoons Al_2O_3 + 3\,H_2 \tag{2.4}$$

at standard conditions has much more driving force ($\Delta G^o_{rxn} = -864.6$ kJ/mol) than the combustion

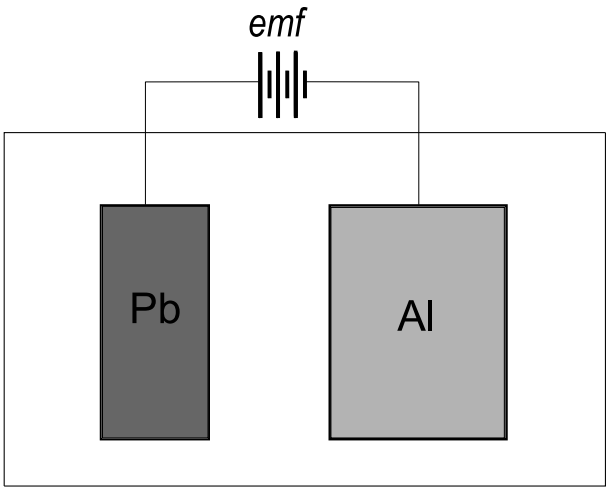

Figure 2.4: A typical anodization setup in which direct current is applied to aluminum in an acidic electrolyte.

of hydrogen. What this means is that the driving force for the oxidation of aluminum is greater than the driving force that destroyed the Hindenburg. However, in normal atmospheric circumstances, aluminum remains mostly zero-valent, with the exception of a very thin oxide layer. The interrelated reasons that aluminum does not readily corrode under normal circumstances are (1) the oxide layer prohibits the flow of electrons from the zero-valent aluminum and (2) the aluminum oxide is mostly insoluble in the electrolyte (*i.e.* water). If this (insulating) oxide layer were pure and defect-free, then oxidation might never proceed to any measurable extent. However, due to the presence of trace metallic impurities (for example, copper and iron at approximately .005 wt%), an electrical circuit exists between the surface and the zero-valent aluminum, which allows for the very slow corrosion of aluminum in exposure to water. [45–47] Furthermore, because of the small thickness of the oxide layer, the metal is susceptible to attack *via* any defect (*e.g.* atomic vacancy, slip) that may be present in the oxide film. [48]

The type of the acid and electrolytes appear to dictate whether the oxide film is dense and thin or porous and thick. In every anodized film, a thin barrier layer exists. When anodizing occurs at neutral pH values and in electrolytes which are poor solvents for aluminum oxide, *only this barrier layer exists* at the surface. Among the most common of these electrolytes is boric acid, but others are possible–including solutions of citrates, tartrates, and phosphates. This anodizing yields a nonporous barrier layer of a few hundred nanometers. [46, 47, 49] If anodizing occurs in strong

acids which sparingly dissolve some of the products of aluminum oxidation (common acids used in this manner are sulfuric, oxalic, and phosphoric), however, the mechanism is much more complex and *results in the formation of a much thicker (up to 200 micrometers) oxide layer (in addition to the barrier layer) that consists mostly of pores* which are capped by the barrier layer. During anodizing, electrons are forced through the oxide layer, and this surplus of electrons enables the initially thin (apprx. 10 nm), relatively dense barrier oxide film to grow to a much thicker (100+ μm), porous film by the effective penetration of electrons through the surface, followed by the removal of elemental hydrogen. Hydrogen is released from the surface *via* formed pores, [46, 47] and it is these pores which give this method much of its relevance to nanoscience and surface chemistry. A typical microstructure is shown as Figure 2.5.

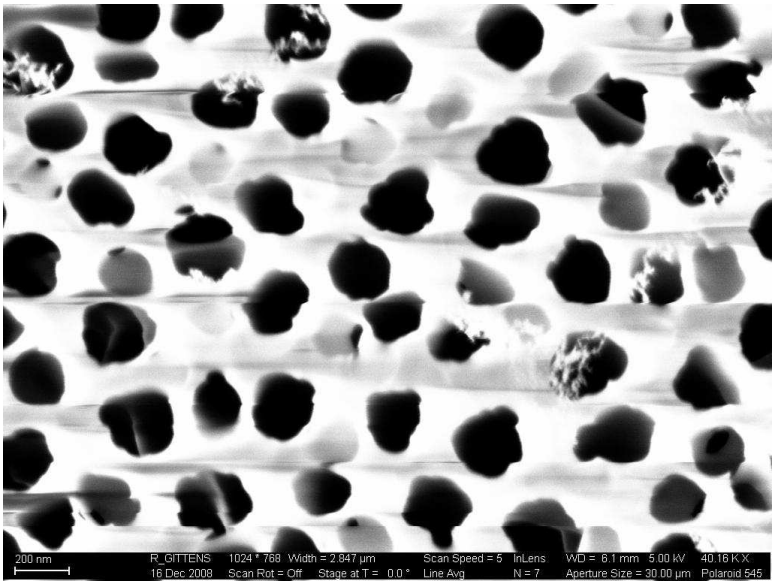

Figure 2.5: Typical porous microstructues are seen after anodizing aluminum. The white bar in the lower left corner represents 200 μm.

In the most idealized case, this porous layer consists of uniform, hexagonally-packed cells (10-500 nm each) which each contain a single pore (diameter of 5-400 nm) that penetrates through the length of the layer. An analogy to wooden pencils whose graphite has been removed can be invoked here. [45] The empty centers would be the pores, and the wood of one pencil would be a cell. The cells organize regularly, due to their hexagonal nature. This idealization is sometimes partially observed in practice, as shown in Figure 2.5, a scanning electron micrograph of an actual anodized alumina film.

The general structure appears to roughly resemble the idealization. It should be noted, however, that this phenomenon does not occur in even some electrolytes which do dissolve aluminum oxide. Depending on treatment conditions (temperature, acid strength and concentration, potential, etc.), separate phenomena, such as pitting, uniform oxide dissolution, and the formation of non-ordered pores may occur in addition to the formation of regularly ordered pores. [47]

The anodization process can be controlled such that pore size can be effectively engineered during synthesis. Furthermore, templating can be used in order to form substrates of identical geometry from different materials. This engineering will be discussed in greater detail in Chapter 7.

CHAPTER III

MATERIALS AND METHODS

3.1 Chapter Overview

Relevant chemicals are introduced, including the polymers, solvents, substrates, and nanoparticle precursors used in this work. Also, experimental techniques relevant to the synthesis, characterization, property analysis of the composites are explained.

3.2 Materials

Anodized aluminum oxide discs (Anodisc) as described in Chapter 2 having a diameter of 13 mm were purchased from Whatman (a unit of GE Healthcare). The membranes featured open cylindrical pores of narrow size distribution and differed in pore size. The pore diameters as reported by the manufacturer were 20 nm, 100 nm, and 200 nm. Independent SEM analysis has determined the mean diameter of these films to be 32 nm, 100 nm, and 220 nm. These discs were determined to be amorphous by x-ray diffraction, and their specific surface areas were calculated by analysis of the scanning electron micrographs shown in Figure 1. It is important to note that the convex (disc circumference) and flat (disc faces) surface areas are negligible because they account for less than 0.3% of the entire surface area on the disc. Therefore, at least 99.7% of all the surface area on the disc resides in cylindrical pores and is concave. The table in Figure 1 shows significant geometric properties of the discs examined in this work.

Poly(methyl methacrylate), PMMA, polymers were purchased from various vendors (Sigma Aldrich Chemical Company, Fisher Scientific, Polysciences, Inc., and Scientific Polymer Products), and their molecular weights are 15000, 75000, 120000, 350000, and 996000 g/mol. Polydispersity indices were generally approximately 1.5. Cellulose acetate propionate of weight-average molecular weight 75,000 g/mol (CAP) was purchased from Sigma Aldrich Chemical Company $DS_{propionyl}$=2.5, DS_{acetyl}=0.2. Polystyrene-block-Poly(methyl methacrylate), PS-b-PMMA, diblock copolymers were purchased from Scientific Polymer Products, and their block molecular weights

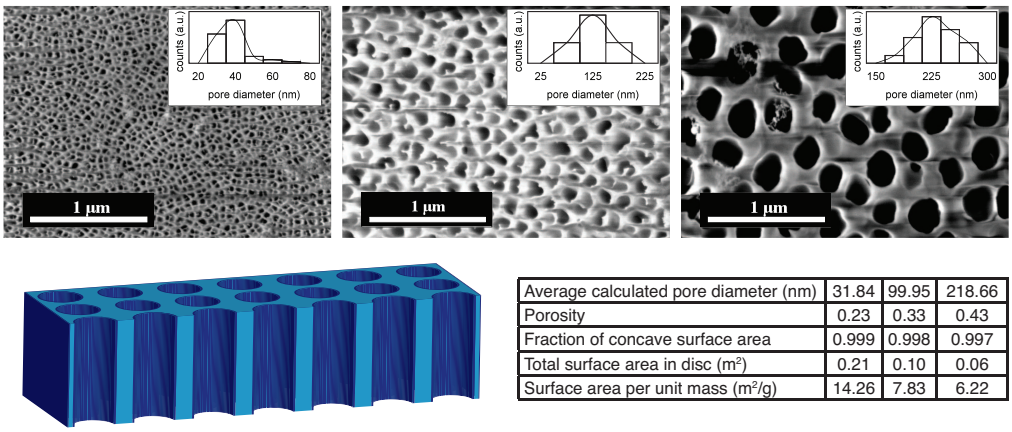

Average calculated pore diameter (nm)	31.84	99.95	218.66
Porosity	0.23	0.33	0.43
Fraction of concave surface area	0.999	0.998	0.997
Total surface area in disc (m^2)	0.21	0.10	0.06
Surface area per unit mass (m^2/g)	14.26	7.83	6.22

Figure 3.1: Clockwise from top left: SEM micrographs of 32, 100, and 220 nm porous media; table with relevant geometries of the substrates; graphical representation of the porous substrates analyzed in this work.

and polydispersity indices are shown in 5.3.

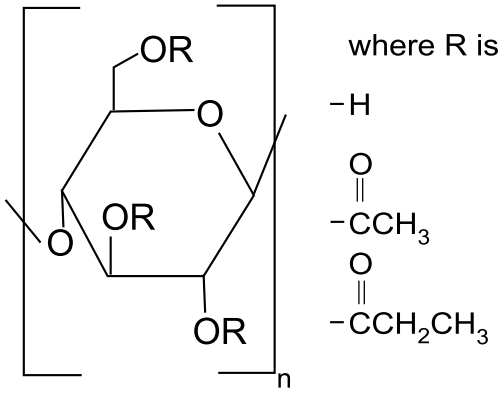

Figure 3.2: The structure of cellulose acetate propionate. Not all of the original cellulose OH groups are converted in the esterification process, and esterification may occur at any of the three original OH positions.

Solvents used in this study were purchased from Sigma Aldrich Chemical Company and used without further preparation unless otherwise noted. Physical data relevant to Chapter 5 can be found in Table 3.2.

Iron, cobalt, and ruthenium carbonyls were used for nanocomposite syntheses. Important physical properties are listed in Table 3.2.

Table 3.1: Solvents Used in this Study

Solvent	Hildebrand solubility parameter [50] $MPa^{\frac{1}{2}}$	Density at 25° C g/cm^3	Intermolecular hydrogen bonding [50]
2-ethoxy ethanol	21.5	0.930	moderate
cyclohexanone	20.3	0.948	moderate
toluene	18.2	0.867	poor

Table 3.2: Metal Carbonyls Used in this Study

Name	Forumla	Specific gravity at STP	Molecular weight g/mol	Phase at STP
Iron pentacarbonyl	$Fe(CO)_5$	1.45	195.9	liquid
Dicobalt octacarbonyl	$Co_2(CO)_8$	1.87	342.0	solid
Triruthenium dodecacarbonyl	$Ru_3(CO)_{12}$	2.48	639.3	solid

3.3 Methods

SEM imaging of the uncoated discs was accomplished by mounting them to a conductive stage with conductive powder and analyzing them under a Zeiss SEM Ultra60 at 5 kV with an in-lens secondary electron detector. X-ray diffraction measurements were performed with a Xpert Pro Alpha-1 (copper source, wavelength of 1.54 Å).

Solutions having concentrations of 15% and 1% (w/v) PMMA or PS-b-PMMA diblock copolymer were prepared by adding appropriate masses of dry polymer to volumetric flasks, filling to the to-contain line with chlorobenzene (99.5%, Acros), and allowing at least 2 days for complete dissolution.

Adsorption of PMMA and copolymers thereof to the surfaces was achieved by the following process: Each disc was exposed to 3ml of polymer solution after the alumina disc and the glass sample vial were rinsed twice with clean solvent. The vials were placed in a laboratory oven at 343K, sealed after their temperature equilibrated, and tilted so that both faces of the disc would be accessible to the polymer solution. Each trial was repeated in triplicate, and the durations of the experiments were 1 day, 3 days, or 7 days.

Before data acquisition, PMMA-rich discs were rinsed in order to remove unbound polymer. Each disc was cooled, removed from its vial, and rinsed at least five times with at least five milliliters

of pure solvent in a Soxhlet extraction apparatus. The disc was removed and examined visually upon drying. If the disc dried unevenly or showed shiny spots on its surface, it was rinsed again in the apparatus in order to remove all unbound polymer. Discs with dirt or other contaminants were discarded.

After ensuring that all discs were viable and free of unbound polymer, their decomposition profiles were measured in a TA Instruments Q50 thermogravimetric analyzer (TGA). Each disc was heated at 20 K per minute from room temperature to 720 K in oxygen. The decomposition profile of the very thin adsorbed PMMA layer matched well with the decomposition profile of bulk PMMA. A typical decomposition plot is shown in Figure 2. Polymer adsorption was determined by the mass loss between 373K and 720K. In this temperature range, the substrate's mass was shown to be constant in a separate experiment.

In a typical nanocomposite synthesis, 4.0 g of cellulose acetate propionate was added to a 100 mL volumetric flask, which was filled with butyl butyrate. This fluid, along with a magnetic stirring bar, was poured into a 100 mL three-neck flask, equipped with a magnetic stirrer, a thermometer, a condenser, and a septum stopper. Depending on the experiment, a specific gas (either oxygen or nitrogen) was bubbled through the fluid at 15 mL/min for at least five hours before reaction at room temperature.

This sealed, purged flask was heated to 150 ^{o}C, and 7.6 mM filtered iron pentacarbonyl, $Fe(CO)_5$, 99.5% (195.895 g/mol, 1.49 g/cm^3) was added to it. This temperature was maintained until the $Fe(CO)_5$ carbonyl peaks in the infrared were no longer observed. The specifics of the above reaction procedure were modified as necessary to accommodate various experimental variables (*e.g.* the identity of the metal carbonyl). For example, triruthenium dodecacarbonyl, which is a solid at room temperature, was dissolved in butyl butyrate before its addition to the polymer solution.

Aliquots were removed via syringe through the septum stopper before, during, and after the reaction. The samples were analyzed via viscometry and Fourier transform infrared (FTIR) spectroscopy. The progress of the thermally-induced decomposition reaction was monitored by infrared spectroscopy. For liquid specimens, KBr windows surrounded a 250 μm liquid film, which was analyzed in a Thermo Nexus 670 infrared spectrometer. For each specimen, 128 scans were taken at a resolution of 2 cm^{-1}, and concentration was correlated to absorbance by Beer's Law. Viscosity was

used to measure the resistance to flow of the fluids during $Fe(CO)_5$ thermolysis and was determined with a Haake model RV20 viscometer with an NVST-II spindle and cylinder at 22 ^{o}C.

CHAPTER IV

THE ADSORPTION OF HOMOPOLYMERS TO CONCAVE SURFACES

4.1 Chapter Overview

This chapter analyzes influence of polymer molecular weight and surface curvature on the adsorption of polymers onto concave surfaces. Polymethyl methacrylate (PMMA) of various molecular weights was adsorbed onto porous aluminum oxide membranes having various pore sizes, ranging from 32 to 220 nm. The surface coverage, expressed as repeat units per unit surface area, was observed to vary linearly with molecular weight for molecular weights below 120000 g/mol. The coverage was independent of molecular weight above this critical molar mass, as was previously reported for the adsorption of PMMA on convex surfaces. Furthermore, the coverage varied linearly with pore size. Theoretical models were explored to describe curvature-dependent adsorption by considering the density gradient that exists between the surface and the edge of the adsorption layer. According to the models, the total coverage increases as particle size also increases, in good agreement with experiment. These results show that the details of the adsorption of polymers onto concave surfaces with cylindrical geometries can be used to calculate molecular weight (below a critical molecular weight) if pore size is known. Conversely, pore size can also be determined with similar adsorption experiments. Most significantly, for polymers above a critical molecular weight, the precise molecular weight need not be known in order to determine pore size. Moreover, the adsorption developed and validated in this work can be used to also predict coverage onto surfaces with different geometries.

4.2 Scope

Polymer adsorption onto surfaces of all geometries is relevant to many fields and applications. One example is the coating of particles with a very thin polymeric layer to provide green strength to ceramic parts before firing (*i.e.*, to serve as a binder in ceramic processing). The nature of the adsorbed

polymer layer (its density and conformation, for example) influences particle packing density, and, therefore, the strength of the final product. [51] Furthermore, it has been shown that polymer adsorption influences the size of nanoscale inorganic particles that nucleate from molecular precursors. [23, 25, 26, 52–54] Adsorption to concave surfaces, the topic of this chapter, is applicable to chromatography. The most obvious example is in the field of adsorption chromatography, wherein the strength of adsorption between molecules and a porous (concave) solid causes molecules to elute at different rates from the stationary phase. [55] Also, although adsorption is undesirable in typical size exclusion chromatography, [56, 57] a similar experiment, in which polymers of known molecular weights are eluted through a porous analyte, can determine the structure of the porous stationary phase. This technique is particularly relevant when studying swollen gels, which are difficult to analyze by traditional porosimetry. [58] Also, modulation of flow through porous media has been proposed for use as a sensor and a valve for fluid flow because the adsorbed layer changes thickness with both solvent quality and flow rate. [59, 60] Furthermore, it will be shown in this paper that polymer adsorption onto concave surfaces can measure the molecular weight or the conformation of the adsorbing chains.

The extent of of polymer adsorption onto porous aluminum oxide after immersion into polymer solutions was measured. Alumina films with three different pore sizes were analyzed, and coverage (a parameter that is proportional to the mass of polymer adsorbed per unit surface area) was shown to decrease as pore size also decreased. We rationalized this result by developing a model that shows that geometric confinement at some distance away from the surface limits the number of polymer chains that can be adsorbed to a concave surface. Of course, as curvature decreases (*i.e.* as radius increases and the surface becomes more flat), the adsorption behaves identically to flat surfaces. The very small polymer "sees" a very large pore as if it were a flat surface for the same reason that we usually see the earth as flat.

A model has been developed, which, supported by experimental data, accurately describe the chemisorption of poly(methyl methacryalte) (PMMA) and onto alumina particles of various sizes. This model is based on two competing processes: (1) The energetically favorable bonding that occurs between the polymer and the surface, and (2) The mutual repulsion of chain segments that

reside in the proximity of the metallic surface. The latter process, which is essentially entropy-driven, varies with surface curvature. For small magnitudes of the curvature (*i.e.*, for large particles), this term is practically identical to that observed for flat surfaces. For medium-sized particles, those having approximately the same size as the radius of gyration of the polymer, this confinement energy changes, resulting in an inverse scaling of the adsorption coverage with the curvature. At very small particle sizes, having dimensions that are much less than the radius of gyration of the polymer, the number of chains bound to the surface is identical regardless of molecular weight, because the polymer chains extend outwardly, again due to the change in the entropic term. [40–42]

In this chapter, I explain, both experimentally and theoretically, the adsorption of polymers onto concave (as opposed to convex) surfaces, in order to shed new light upon the nature of curvature-dependent adsorption. Experimentally, the chemisorption of PMMA onto various concave aluminum oxide media was analyzed in order to determine the effects of both polymer molecular weight and curvature on the adsorption process. The Al_2O_3-PMMA system was chosen because of its well-understood mechanism of adsorption. This mechanism is characterized by the de-esterification of the side group, followed by the interaction of the resultant conjugate base with a positively-charged aluminum atom on the surface in the presence of a minimal amount of water, as shown in Figure 4.1. [61–65]

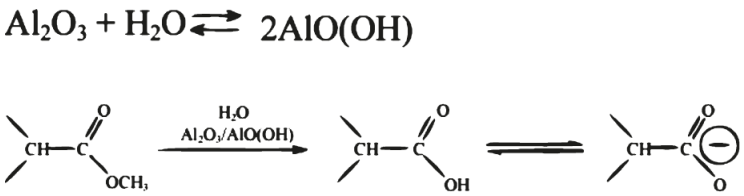

Figure 4.1: The adsorption of PMMA to alumina. The bonds between the COO^- groups on the PMMA and the Al3+ sites on the surface are formed by two subsequent reactions: (1) conversion of Al2O3 to AlO(OH) on the surface of the adsorbent in the presence of H2O and (2) de-esterification of the methacrylate group in the presence of the surface OH groups to form the carboxylate group.

Polymer chains that are unbound to the surface can be rinsed away, allowing for the analysis of only those chains in which at least one repeat unit is in intimate contact with the surface. The Al_2O_3 concave surfaces consist of porous sheets with different pore sizes, as shown in Figure 1(a-c). While the effective cavities in which the adsorption takes place in this case are cylinders, the

concavity of the system is two-dimensional, and hence the theoretical application of the previously-developed model is altered accordingly. [40] Therefore, the goal of the work is to relate experimental measurements of polymer coverage onto these cylindrical surfaces to theoretical predictions.

4.3 Results and Discussion

It is well known that adsorption kinetics are generally slow when the adsorbent is porous. [66] So the kinetics of adsorption were investigated for this system in order to determine when steady-state conditions were achieved. It was determined that a duration of three days was necessary to achieve saturation in all of these systems and that the kinetics of adsorption were indicative of equilibrium (as opposed to mere steady-state conditions), which implies complete, exhaustive coverage over all surfaces, thereby justifying the calculations of coverage. As can be seen by plotting the duration of experiment *vs.* coverage for two different molecular weights and three different pore sizes, shown in 4.2, saturation appears complete by 3 days for all systems analyzed. Furthermore, equilibrium conditions - and not steady-state conditions - were determined to occur because saturation was reached faster in the lower molecular weight system and on the same time scale for both large and small pore sizes and large and small molecular weights. It was assumed that the only way to prevent equilibrium conditions from occurring is clogging, in which the local concentration of polymer chains inside a pore is so great that subsequent chains cannot penetrate this mass in order to access the interior, uncovered surfaces. Such clogging, if it were to occur, would indicate that calculations of coverage were artificially low. However, because of the observed saturation kinetics, shown in Figure 3, clogging did not occur. If clogging would have occurred, saturation would be reached faster in systems with smaller pores and in systems with higher polymer molecular weights, much for the same reasons that a smaller drain would be clogged more easily than a larger drain and that long hair would clog a drain more easily than short hair. Also, if plugging were to occur, lower molecular weights would feature less plugging and would have more mass adsorbed to the surface; however, the opposite trend was observed, presumably due to the higher mobility of the smaller chains. [66] The data show that plugging does not occur, thereby indicating the equilibrium state of the system at saturation.

The achievement of equilibrium is a critical assumption in this work, and it has been confirmed

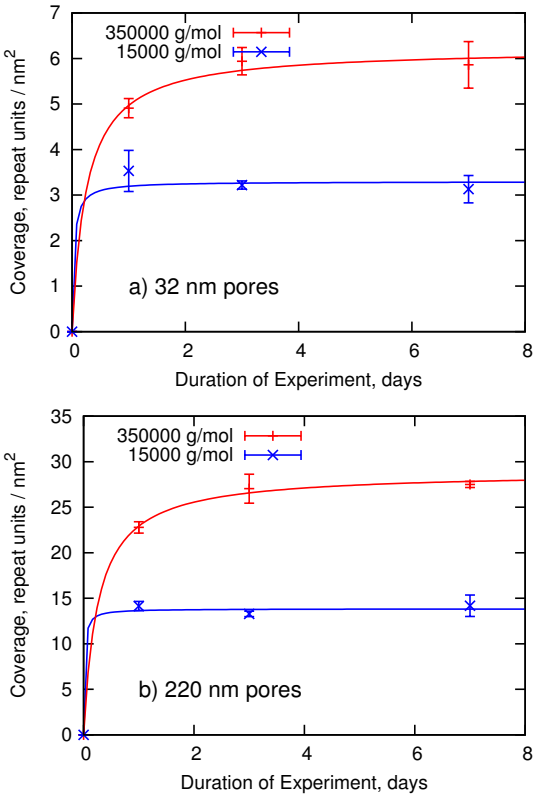

Figure 4.2: Adsorption kinetics for both high (350000) and low (15000) molecular weight PMMA adsorbed to 32 nm (a) and 220 nm (b) pores. Because of the kinetics of these systems as well as other reasons described in the text, equilibrium is assumed to be achieved.

by additional methods other than the saturation argument outlined above. After three days of exposure of 32 nm pore size discs to 350000 g/mol PMMA, the discs were cleaned as usual and subjected to 10 minutes of ultrasound treatment in pure solvent, followed by reinsertion of new polymer solution. If plugging were to occur, more mass adsorbed would be expected on the discs after this treatment. No such increase was observed.

In addition, a separate experiment was designed to determine the role of diffusion on the adsorption process. In this experiment, both oven-dry and wet-with-solvent 32 nm, 100 nm, and 220 nm discs were exposed to PMMA solutions having a PMMA molecular weight of 120000 g/mol. If plugging were to occur, the wet-with-solvent discs should adsorb less mass than the oven-dry discs because, in the latter case, the concentration of polymer inside the pore is instantaneously identical at all locations (because of fluid flow), as opposed to the former case, in which uniform concentration across the pore length is gradually achieved by the diffusion of polymer through solvent. No such differences were observed as the measurements were statistically identical. Furthermore, a logical argument using previously collected data supports the equilibrium argument. If plugging were to occur, almost all of the pores' surface area would be inaccessible to the polymer. In such a case, assuming the coverage to be on the same order of magnitude as adsorption to flat surfaces, [40] the mass adsorbed would be so small as to be practically immeasurable, given the precision of the TGA balance. All of these arguments, in addition to the saturation argument described in the previous paragraph, indicate that equilibrium is reached.

In previous studies, [40–42] it has been shown that the coverage of the polymer on convex surfaces was dependent only on the curvature and independent of the polymer molecular weight. However, in the concave case, a plot of coverage *vs.* polymer molecular weight, shown in 4.3, clearly demonstrates the existence of two distinct adsorption regimes: A molecular weight-dependent regime and a regime in which adsorption is independent of molecular weight. At 120000 g/mol and below, the adsorption per unit surface area appears to vary linearly with polymer molecular weight. This linear dependence can be seen more easily in 4.4.

The slopes of these lines at low values of molecular weight (below 120000 g/mol), *i.e.* the linear variation in coverage with polymer molecular weight, will be referred to in this paper as the specific molar coverage. As shown in Figure 6, the specific molar coverage increases with the increase in

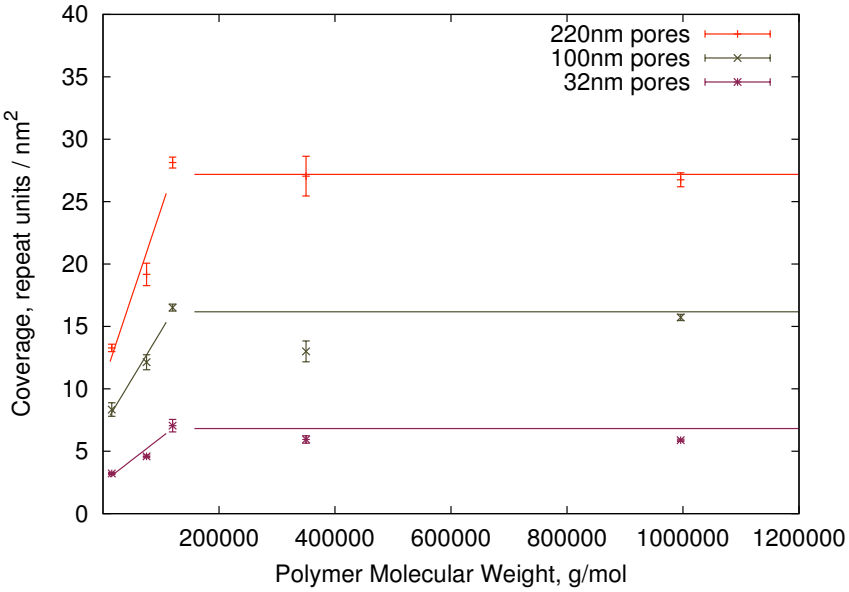

Figure 4.3: Coverage in repeat units per square nanometer *vs.* molecular weight for the three different pore sizes. Notice the molecular weight-dependent regime and the molecular weight-independent regime.

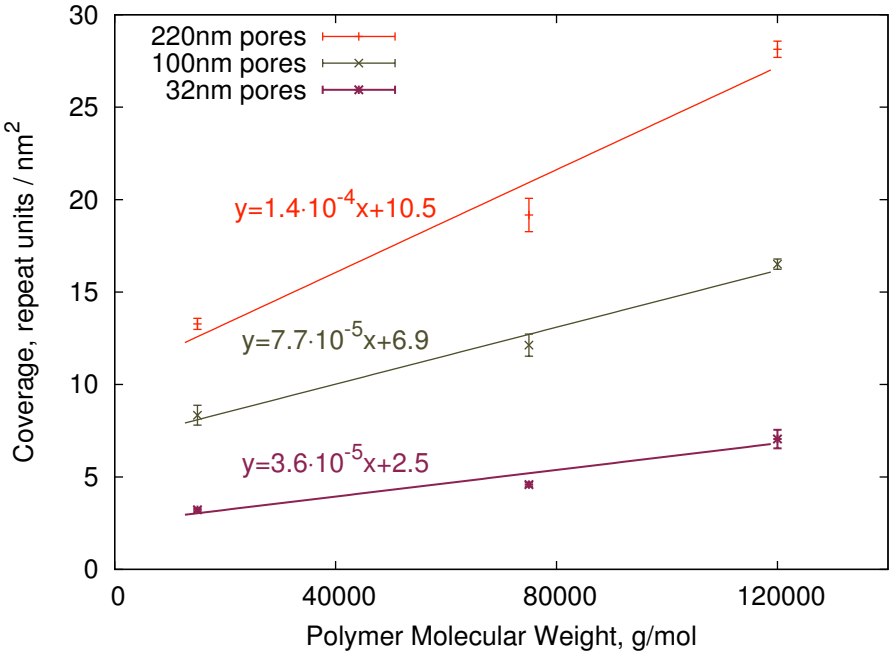

Figure 4.4: Coverage *vs.* molecular weight at low molecular weights. An enlargement of the molecular weight-dependent regime of the previous figure.

pore size. An explanation of this phenomenon may be rationalized in the following manner: Above a critical polymer length regime, the adsorption layer would have a width L and a constant coverage, regardless of the length of the polymer chains, even if shorter chains will have a smaller number of contact points per chain with the surface, as shown in 4.6 a. [67] When the polymer chain length decreases such that it has the precise length to form a brush with length L, the adsorption will exhibit one contact point per polymer chain, as shown in 4.6 b. For even shorter polymer chains, the single anchoring point per chain with the alumina surface still remains valid, forcing the formation of an adsorption layer with a width that is less then L, as shown in 4.6 c. In this polymer length regime, the coverage will decrease and will be proportional to the length of the chains, *i.e.* to the mass of the polymers. It is important to note that the dependence of adsorption on polymer molar mass is not identical for every system, [66, 68] and care must be taken to avoid over-generalization of system-specific results. Although the dependence of the specific molar coverage on pore size appears to be linear, a definitive relationship is elusive with the current minimal data set. Additional data points are required in order to assess the nature and universality of this dependence.

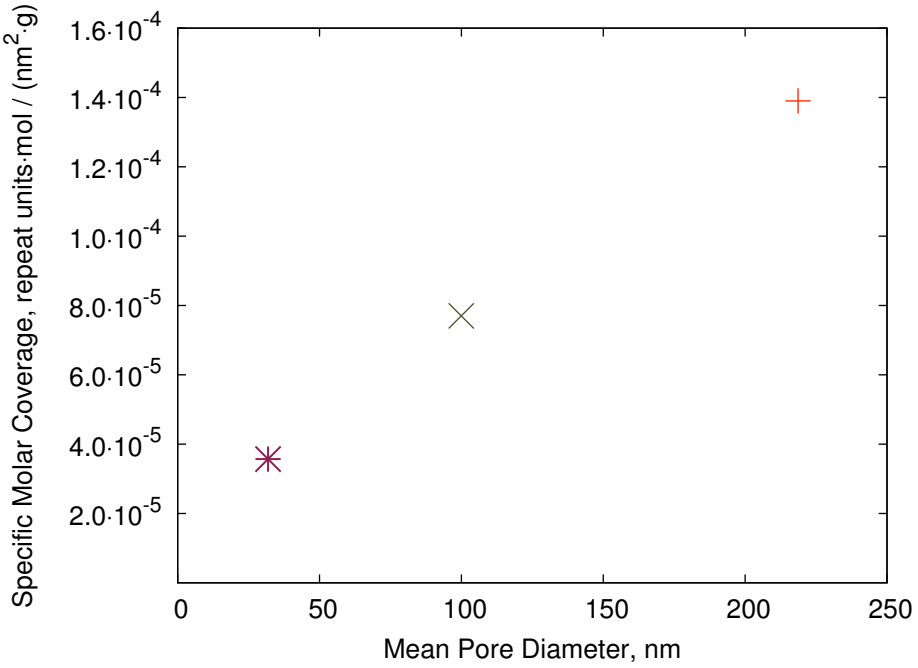

Figure 4.5: An apparently linear relationship exists between the slopes of the lines of the previous figure plotted and pore size.

A similar relationship can be seen when examining the effect of polymer concentration on coverage, as shown in Figure 8. In this case, the dependence of the adsorption on pore size seems to be linear (as expected from the previously-developed model [40]), and the slope changes with polymer concentration. Polymer chains are more likely to leave the solution for the surface in the more concentrated system. During adsorption, dissolved PMMA is in equilibrium with PMMA that has precipitated onto the surface, and hence, an increase in dissolved PMMA concentration will result in more PMMA adsorbed onto the aluminum oxide surface.

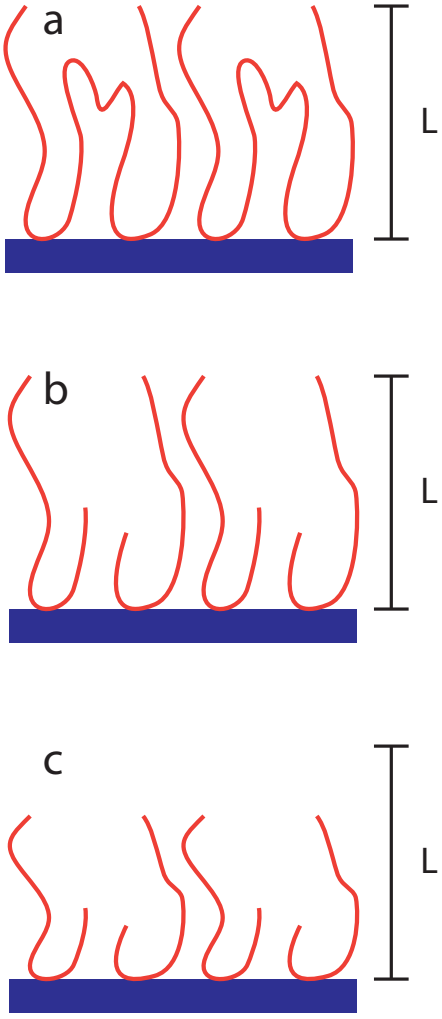

Figure 4.6: The graphical explanation of the molecular weight-independent region in Figure 4.3. The thickness and density of the adsorbed layer do not significantly change between very high molecular weights (a) down to 120000 g/mol (b), below which the adsorption blobs decrease in size with a decrease in molecular weight (c).

The implication of these relationships among the specific molar coverage, the pore size and the

polymer concentration in solution indicate that the adsorption of PMMA onto anodized aluminum oxide media can be used as a direct measure of either molecular weight or pore size if the other is known. For example, PMMA molecular weight (below 120000 g/mol) can be measured by adsorbing it to commercially available anodized aluminum oxide discs of known pore size. Likewise, pore size of anodized aluminum oxide can be measured by using it as a substrate for the adsorption of PMMA of known molecular weight. In fact, for large polymers, the molecular weight must not be known accurately in order to determine pore size, due to the independence of the adsorption on polymer size in this molar mass regime. The importance of a new way of measuring molecular weight is obvious, but the significance of measuring pore size requires some explanation. These membranes were fabricated by the anodization of aluminum, a process that is known to yield open, cylindrical pores. Depending on the anodization conditions (*e.g.*, acid strength, voltage, and temperature), pore size varies and is often too small to measure with a conventional light microscope. [69] Therefore, after fabrication of such anodized aluminum oxide media, pore size could be measured directly by a simple adsorption experiment, rendering traditional pore size measurement tools, such as electron microscopy, porosimetry, and gas adsorption unnecessary (especially if such methods were prohibitive or unavailable).

4.4 Theoretical Approach

As mentioned in Chapter 2, the adsorption of PMMA onto alumina occurs because of an energetic gain from this process because the polymer chain has some attraction to surface. However, it comes at a loss of conformational entropy because of the impenetrable surface. Let us now conduct a simple thought experiment to understand why a decrease in pore size down to the nanoscale would lead to a decrease in coverage. Assuming that the adsorbed layer consists of an array of blobs of diameter ξ_{ads}, as proposed by Rubinstein, [67] the thickness of the adsorbed layer will be ξ_{ads}. Assuming that blob height and, therefore, the thickness of the adsorbed layer do not vary with surface curvature (This assumption is questionable (*vide infra*); nevertheless, this model remains instructive.) To simplify the model, the adsorption blobs are assumed to be cubic, as shown in figure 4.7. These squares are assumed to be hard (*i.e.* their overlap is forbidden). The coverage, therefore, within a pore of radius *r* can be determined mathematically:

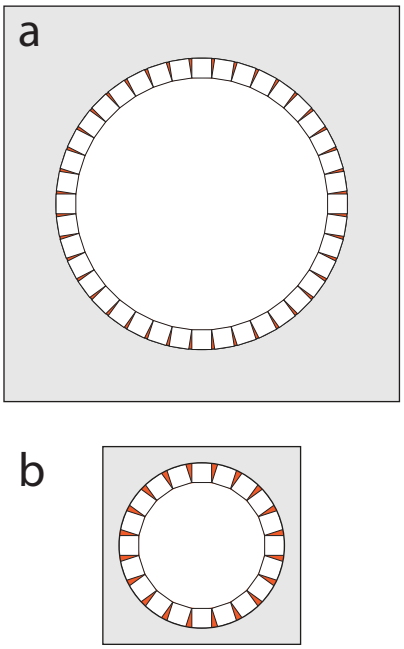

Figure 4.7: The model described in this section predicts a significant decrease in polymer coverage with a decrease in pore size because of excluded surface area for small pores (b), due to a constant size of adsorption blobs.

The coverage is equivalent to the mass of one blob multiplied by the number of blobs on a surface, divided by the surface area of the pore:

$$\Gamma = \frac{m_b N_b N A}{2\pi r \xi_{ads} F W} \tag{4.1}$$

where m_b is the mass of one blob and N_b is the number of blobs that are allowed within a cylinder with radius r and thickness ξ_{ads}. Avogadro's number is N_A, and FW is the molar mass of one repeat unit of the PMMA repeat unit.

In this model, ξ_{ads} is assumed to be constant. N_b, the number of blobs on the surface, due to energetic constraints, will vary with r, and this relationship can be determined mathematically:

$$N_b \xi_{ads} = 2\pi(r - \xi_{ads}) \tag{4.2}$$

This expression simply means that an inner circle can be approximated by connecting the inner-most edges of blobs and that the circumference of this inner circle can be determined by multiplying the number of blobs, N_b, by the width of a blob, ξ_{ads} and also by multiplying π by the diameter of the inner circle. Thus N_b is determined to be:

$$N_b = 2\pi\left(\frac{r}{\xi_{ads}} - 1\right) \tag{4.3}$$

Substitution of 4.3 into 4.1 yields:

$$\Gamma = \frac{m_b N_A}{\xi_{ads} FW}\left(\frac{1}{\xi_{ads}} - \frac{1}{r}\right) \tag{4.4}$$

In this model, m_b is assumed to be constant, as is ξ_{ads}. Both N_A and FW will always be constant, regardless of the model. Therefore, we can safely say that

$$\Gamma \propto A - \frac{B}{r} \tag{4.5}$$

A plot of the type of Equation 4.5 can be seen in Figure 4.8, which uses a known values of ξ_{ads} (8.7 nm) observed for adsorption of PMMA onto a flat surface. [64]

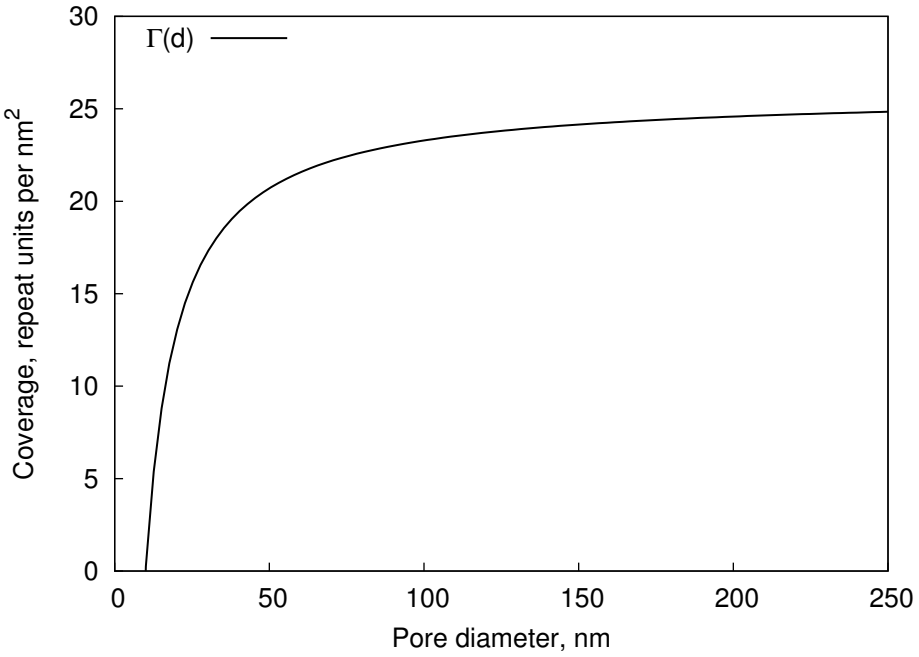

Figure 4.8: Theoretical coverage, Γ, as a function of pore diameter, d.

Note the general shape of the function. Due to energetic constraints, the system cannot support any blobs at a pore diameter smaller than 2 ξ_{ads}. Furthermore, as pore size increases, the plot

rapidly approaches an ultimate value, which shall be called Γ_{max}, whose value is straightforwardly determined:

$$\Gamma_{max} = \lim_{d \to \infty} \Gamma = \frac{N_A m_b}{FW\xi_{ads}^2} \tag{4.6}$$

The value of m_b can be determined from measured values of Γ_{max} and ξ_{ads}, which have been determined for this work and reported in the literature as 25.92 repeat units per nm^2 and 8.7 nm, [64] respectively. This calculation yields a result of m_b = 3.28 x 10^{-19} g. Important parameters that can be deduced from this value are blob and, therefore, adsorbed layer density, ρ and the number of repeat units per blob: 0.5 g/m^3 and 1975 repeat units, respectively. It is important to note that the value of ρ can be calculated from the measurements in [64] and that the density of PMMA at the alumina surface is much less than the bulk density of PMMA (1.19 g/cm^3 [50]).

Despite the instructive utility of such a model, it is nonetheless deficient. Blob thickness, ξ_{ads}, is not constant for any given system of varying curvature. The above model assumes that blob size, ξ_{ads}, does not change with pore size. However, this assumption is questionable. Previous experimental and theoretical work has shown that a change in curvature in the convex surface-PMMA system leads to changes in both ξ_{ads}. [70] In order to address these deficiencies, a previous model [40–42] has been modified that needs not make such assumptions. [71] For completeness, this model will be discussed here.

Because the experimental results reported in this manuscript show such a remarkable resemblance to the experimental results obtained for the adsorption of PMMA onto spherical convex surfaces [40–42], the model developed for that particular system was used as a foundation for describing this system. On both concave and convex surfaces, it was demonstrated that the coverage per unit surface area is roughly proportional to the radius of the spherical particles and independent of the molecular weight of the polymer. The assumptions of this model are as follows: (a) Semi-dilute polymer solutions; (b) Small adsorption energy per repeat unit; (c) Low coverage of the surface with directly adsorbed (anchored) repeat units; (d) The radius of curvature of the adsorbent surface was larger then the two typical lengths of the problem, *i.e.* the polymer radius of gyration and the typical width of the adsorbed layer. This was pertinent to all systems with the exception of those having very small radii (apprx. 5 nm in diameter), which were not duplicated for the concave

case.

This similarity indicates that both cases of adsorption, *i.e.* on concave and convex surfaces, exhibit a universal behavior that describes the adsorption on any curved surface. Existing theory for the adsorption on polymers on spherical particles that is based on scaling arguments [72] predicts that for the same experimental setup, the coverage should be independent of the size of the adsorbed particle. This result stands in a complete opposition to previous experimental results, which show a rough linear dependence of the coverage on the radius of curvature. In a previous study, the discrepancies between the theory and the experimental results were explained by adding an additional force term that was proportional to the monomer density gradient. The outcome of this force was a repulsion of the adsorbed polymer chains away from the surface. It has been shown that for spherical particles, the density gradient in the adsorption layer is proportional to 1/R where R is the radius of the adsorbing particles. This term imparted a positive addition to the free energy of the adsorption layer, which was increasing linearly with the curvature, resulting in the contraction of the adsorption layer.

Here the same construction is applied to develop a density gradient term for the case of the adsorption of polymer chains on the inside surface of a cylinder. For the clarity of the explanation a model [72, 73] is used that approximates the loop distribution in the adsorption layer with a brush of disconnected tails, as shown in Figure 9. The adsorbed layer can be assumed to behave as a brush of disconnected tails. Using this assumption, the connecting segments of the loops can be isolated and assumed negligible resulting in an idealized brush.

Figure 4.10 shows the structure of the adsorbed layer in a cross-section of the cylinder. An approximation that was made was that the number of tails in each cylindrical annulus of the adsorption layer was constant and noted by N_R. In actuality, although some of the tails will invariably be shorter than others, [74] this fact will not change the curvature dependence of the gradient term significantly. Each tail was now represented by a sequence of blobs (segments of the freely-coiled chain encased in a sphere), such that the blobs become smaller as a function of their increased distance from the inner surface of the cylinder. The astute reader will note that this blob model is better-defined and more realistic than the square blob model discussed previously. The radius of the largest blob at a distance R from the center of the cylinder is b_R, and the radius of a given blob along

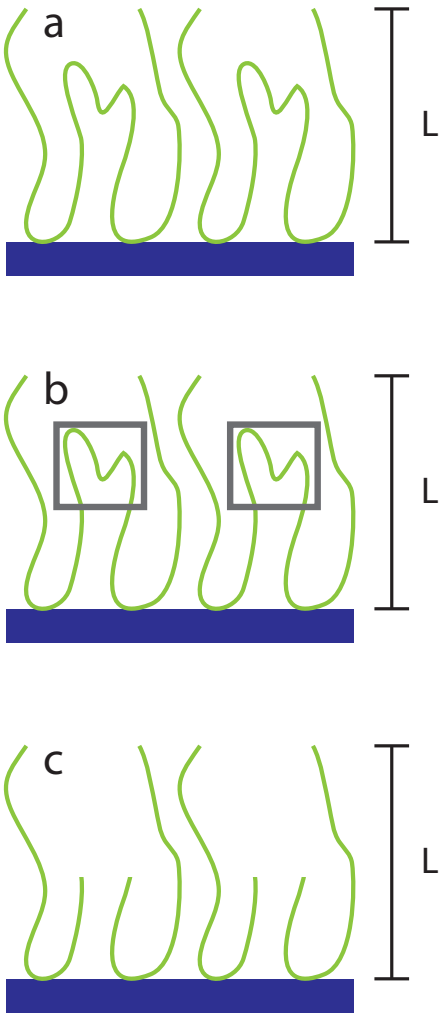

Figure 4.9: The adsorbed layer (a), after removal of parts of some trains (b), can be assumed to be a brush of disconnected tails (c).

the tail at a distance r from the center of the cylinder is b_r. The radius of the blob at distance from the center of the cylinder is given by $b_r = a_0 N_r^{\nu}$, where a_0 is the dimension of a segment of PMMA, N_r is the number of segments constituting the portion of the polymer tail contained in a blob and ν is the Flory coefficient (*e.g.* $1/2$ for a theta solvent and 3/5 for a good solvent). In this development, it will be assumed that $1/2 < \nu < 1$, *i.e.*, the solvent is a good solvent, as the solvent, chlorobenzene, is an excellent solvent for PMMA. The number of segments in a blob of radius b_r at a distance from the center of the cylinder is therefore $N_r = (b_r/a_0)^{1/\nu}$, and the total number of segments that could reside in a blob is given by $\hat{N}_r = (2\pi b_r^2/(2\pi a_0^2) = (b_r/a_0)^2$. Because the radii of the blobs scale as $b_r = b_R(r/R)$ and $b_R = 1/2N_R$, the fraction of 2D sites in an annulus of distance r from the center of cylinder that are occupied by polymer segments is given by:

$$\Phi(r) = \frac{N_r}{\hat{N}_r} = \left[\frac{(b_r/a_0)^{1/\nu}}{(b_r/a_0)^2}\right] = \left(\frac{b_R r}{a_0 R}\right)^{(1/\nu)-2} = \left(\frac{1}{2a_0 N_R R}\right)^{(1/\nu)-2} r^{(1/\nu)-2} \tag{4.7}$$

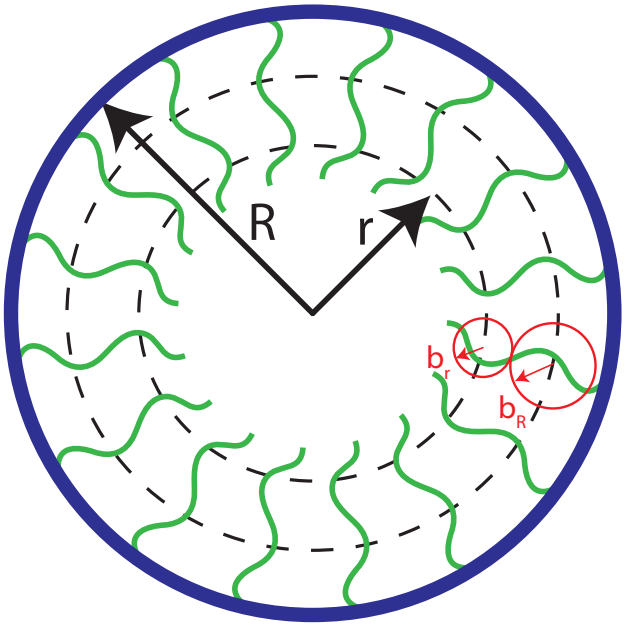

Figure 4.10: Schematic description of the structure of the adsorbed layer in a cross section of the cylinder. R is the diameter of the cylinder, L is the thickness if the adsorbed polymer layer, b_R is the radius of the largest blob directly residing on the surface (at approximately distance R from the center of the cylinder, given that $b_R \ll R$), and b_r is the radius of the blob residing at a distance r from the center of the cylinder.

The fraction of 2D sites occupied by polymer segments, $\Phi(r)$, may be approximated to represent the density of polymer segments in a given annulus of the cylinder. Note that because of the

geometry of the cylinder, it is sufficient to just consider the planar density: The spatial density is simply the planar density divided by the height of the cylinder.

For simplicity, the expression $(1/2a_0N_RR)^{(1/\nu)-2}$ will be replaced by a constant denoted as Z_R. The volume fraction (*i.e.*, density) gradient of 2D sites in a given annulus that are occupied by polymer segments is given by:

$$\Phi'(r) = \frac{d\Phi(r)}{dr} = Z_R\left(\frac{1}{R}\right)^{(1/\nu)-2}\ [(1/\nu)-2]r^{(1/\nu)-3} \tag{4.8}$$

The energy per unit of surface associated with the adsorption of the polymer chains onto the inner surface of the pore (cylinder) is responsible for the density gradient $\Phi'(r)$. As the curvature of the pore increases, the density of the polymer segments in the adsorption layer increases, and hence, $\Phi'(r)$ increases. For a flat surface, the density of segments in the adsorption layer L is constant, *i.e.*, $\Phi'(r) = 0$. The same adsorption energy will have the effect to minimize the density gradient in the adsorption layer of a curved adsorbent surface.12 Therefore, the magnitude of the density gradient $\Phi'(r)$ scales with the curvature 1/R (provided $|\Phi'(r)| \neq 0$).

The total density per unit area can be obtained by integrating the density gradient over the whole adsorption layer *L*. Since it is assumed that $L << R$, the following is true:

$$\Gamma_R = \frac{R}{L}\int_{R-L}^{R}\Phi'(r)r\,dr = \frac{Z_R}{L}\left(\frac{1}{R}\right)^{(1/\nu)-3}\left(\frac{(1/\nu)-2}{(1/\nu)-1}\right)[R^{(1/\nu)-1}-(R-L)^{1/\nu-1}] \approx Z_RR(2-1/\nu) \tag{4.9}$$

The term Γ_R is, by definition, the number of adsorbed repeating units per unit surface area, *i.e.* the total coverage. For a good solvent, $\nu = 3/5$, and hence the total coverage becomes:

$$\Gamma_R = \frac{1}{3}Z_RR = \frac{1}{3}\left(\frac{1}{2a_0N_R}\right)^{(1/\nu-2)} \tag{4.10}$$

Therefore, the theoretical prediction of the linear dependence of the coverage on R matches well, at least qualitatively, with the observed relationship between coverage and pore size (see Figure 8, for example).

4.5 Summary

The adsorption behavior of polymers onto concave surfaces by exploring the equilibrium adsorption of PMMA onto alumina membranes with varying pore sizes. Based on the experimental results for this cylindrical geometry, a mathematical model was developed by considering the polymer density gradient onto the adsorbent surface, *i.e.*, at the inner wall of each cylindrical pore in the membrane. The density gradient of the polymer chains adsorbed on the interior of each such cylinder increases as the distance between the wall and the center of the cylinder decreases, *i.e.*, it is directly proportional to curvature. As a result, the total coverage of the polymer varied linearly with pore size. In addition to its dependence on pore size, the total coverage also was dependent on polymer molecular weight for low molecular weights but independent of molecular weight for high molecular weights, the latter case being similar to adsorption on convex surfaces. The practical implication of these results is that simple adsorption experiments may be used to measure directly both pore size and molecular weight.

CHAPTER V

THE ADSORPTION OF DIBLOCK COPOLYMERS POLYMERS TO CONCAVE SURFACES

5.1 Chapter Overview

The influence of pore size, relative block size, and solvent quality on diblock copolymer (in which one block strongly adsorbs to the surface and the other weakly physisorbs) adsorption was determined. Various PS-b-PMMA copolymers were adsorbed to porous alumina of various pore sizes in order to achieve this goal. It was determined that (much like homopolymer PMMA adsorbed onto the same surfaces) diblock copolymer coverage decreases significantly as pore size decreases. Furthermore, coverage is seen to vary with relative block size and solvent quality according to the anchor-buoy model and deviation from it. This work is significant to the study of block copolymer conformation in solutions and on surfaces, adsorption chromatography, and solvent sensors and controls.

5.2 Scope

The conformation of block copolymers in solution has attracted considerable interest from the scientific community in recent decades, with many accounts directed towards determining the extent of block segregation. [75] The conformation of a diblock copolymer in solution has been researched in the literature. Three solvent-dependent possibilities have been proposed: 1) a dumb-bell conformation, which consists of mostly segregated A and B regions, 2) a psuedo-Gaussian conformation, in which little block segregation occurs, and 3) a core-shell conformation, in which one block surrounds the other block. [76, 77]

The conformation of poly(styrene)-b-poly(methyl methacrylate) (Figure 5.1) has been addressed specifically in the literature. Han and Mozer determined experimentally the radii of gyration the PS and PMMA blocks in PS-b-PMMA (88,000 g/mol (PS block) and 203,000 g/mol PMMA) in toluene

to be 21 nm and 8.5 nm, respectively. Although the PMMA block is over twice as long and massive as the PS block (the molar mass of one repeat unit of PMMA and PS are quite similar, as are their characteristic ratios [50, 78]), the radius of gyration of the PS block was found to be twice that of the PMMA block. A radius of gyration of 8.5 nm for 203,000 g/mol PMMA homopolymer indicates near-theta conditions. Although toluene is a thermodynamically good solvent for PMMA, the authors explained this apparent paradox by considering that toluene is a much better solvent for PS than for PMMA, and, therefore, a core-shell conformation is adopted, with PMMA as core and PS as shell. [79] Clearly, PS-b-PMMA conformation depends upon solvent quailty, and this work discusses the effect of not only solvent quality but also block asymmetry and pore size on adsorption of said block copolymers to porous alumina.

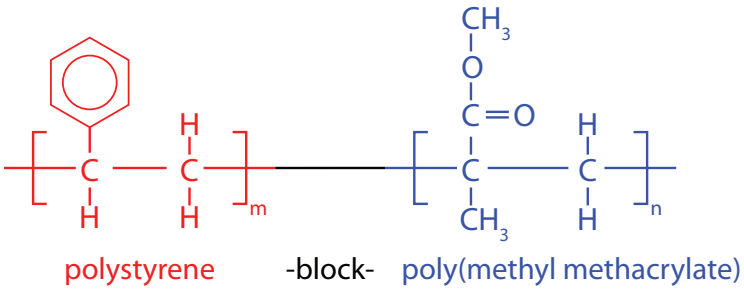

Figure 5.1: Chemical structure of poly(styrene)-b-poly(methyl methacrylate)

Adsorption onto alumina occurs by different mechanisms for PS and PMMA. PS passively associates with the alumina surface, whereas PMMA chemisorbs. The chemisorption of a PMMA repeat unit occurs in the following manner: a side group is de-esterified, and the resultant conjugate base interacts with a positively-charged aluminum atom on the surface in the presence of a minimal amount of water, as shown in Figure 4.1 . [61–65] Polystyrene, however, weakly associates with the surface *via* π bonding of the benzyl group to the surface (Figure 5.2).

The adsorption of homopolymers to concave media (Chapter 4) and the adsorption of homopolymers and diblock copolymers to convex media [40–42] had addressed how polymer adsorption changes as curvature increases. It was discovered that polymer coverage–repeat units per unit surface area–declines significantly as pore size decreases.

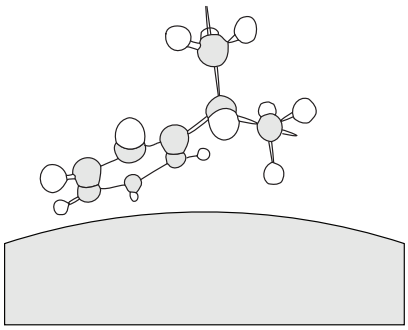

Figure 5.2: Polystyrene interacts weakly with alumina through transient π bonding with the surface, as opposed to the strong bonding observed in the PMMA-alumia system (Figure 4.1).

It is the confluence of these three phenomena (1) solvent-dependent conformation of PS-b-PMMA and 2) chemisorption of the MMA repeat unit to alumina and 3) curvature-dependent adsorption of polymer chains to concave surfaces) that constitutes the scope of this work. In this study, the adsorption of block copolymers to concave alumina surfaces from three different solvents was studied. This chapter describes the adsorption of diblock PMMA-PS copolymers onto concave alumina surfaces of varying curvatures. A theoretical approach was developed as a framework for understanding the adsorption of this particular block copolymer to alumina of various curvatures.

5.3 The Anchor-buoy Model

The anchor-buoy model [75, 80–82] will be used here as an ideal model that describes PS-b-PMMA copolymer adsorption to alumina surfaces. In this model, one block is strongly adsorptive to the surface (in this case, PMMA), and the other block (in this case PS) weakly associates with the surface. In the anchor-buoy model, the strongly adsorptive block associates with the surface. As such, it is referred to as the anchor. The weakly adsorbing block extends outwardly from the surface into the solvent much as the tether that extends to the buoy. The suitability of this model and deviation from it, it will be shown, dictates the adsorptive behavior in this particular system.

Solubility parameters (found in Table 3.2) alone should not be used as guaranteed predictors of solubility. Dipoles, hydrogen bonding, and π-bonding, among other inter- and intra-molecular forces must be considered. [83, 84] The way I have chosen to analyze this system is through polarity. Poly(methyl methacrylate) is much more polar than polystyrene. As such, nonpolar toluene prefers

Table 5.1: Block Copolymers Examined in this Study

Name	PS block molecular weight (M_N) g/mol	PMMA block molecular weight (M_N) g/mol	PDI
low-low (ll)	25000	26000	1.06
high-low (hl)	166200	42000	1.07
high-high (hh)	201500	152000	1.09
low-high (lh)	29200	285100	1.08

the PS block over the PMMA block, and experimental evidence supports this conclusion, as previously mentioned. [79] Likewise, polar 2-ethoxy ethanol is expected to be a good solvent for PMMA and a poor solvent for PS, which experiment also supports. [85] Cyclohexanone, a good solvent for both blocks, is more polar than toluene yet less polar than 2-ethoxy ethanol.

The block copolymers used in this study can be found in Table 5.3.

5.4 Results and Discussion

Two values were calculated from the experimental data: chain density (Ψ) and repeat unit density (Γ). Repeat unit density, referred to interchangably as coverage, is simply the total number of repeat units in all polymer chains that are adsorbed divided by the total surface area, as described in Chapter 4. Chain density refers to the total number of adsorbed block copolymer chains divided by the entire surface area. The value Ψ can be calculated by dividing Γ by the total molecular weight of the block copolymer.

In the previous chapter, the coverage of PMMA homopolymer to porous alumina substrates generally increases with molecular weight up to a threshold, after which it is constant with further increases in molecular weight. Therefore, logical questions to ask here are: how does coverage vary with block copolymer molecular weight, how is this different from homopolymer adsorption, and why?

We can see from a plot of total molecular weight (PMMA block + PS block) *vs.* coverage (Figure 5.3) that, contrary to trends observed for homopolymers, maximum coverage is achieved not for the highest total molecular weight block copolymer. The polymer designated 'HL' shows a greater value of coverage, even though its combined molecular weight is approximately 60%

of the copolymer designated ’HH.’ Furthermore, the copolymer ’LH,’ though its total molecular weight is quite high, does not show a commensurate magnitude of coverage. This is one significant way in which the adsorption of block copolymers on these porous media differ significantly from homopolymer adsorption.

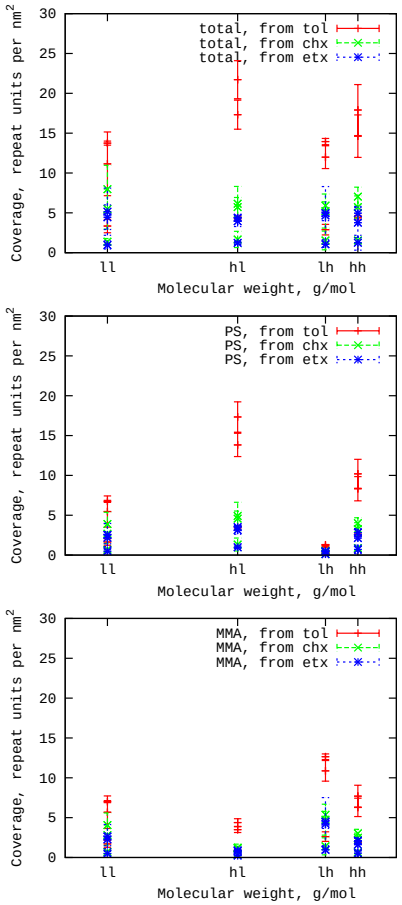

Figure 5.3: Total coverage (top), PS contribution (middle), and PMMA contribution *vs.* total molecular weight.

Another graph that presents identical information as the previous plot (Figure 5.3) is presented as Figure 5.4. This plot shows relative block size with the weighted lines. HH and HL copolymer markers are seen to be half-and-half, while the other copolymers are also weighted appropriately. This graphical presentation shows all relevant data: relative block sizes, coverage, pore size, *etc*. The x axis is total molecular weight (A+B). Solvents are shifted by a common factor and arranged left-to-right in increasing polarity.

It is also possible to plot the same data against A block only (Figure 5.5) and B block only

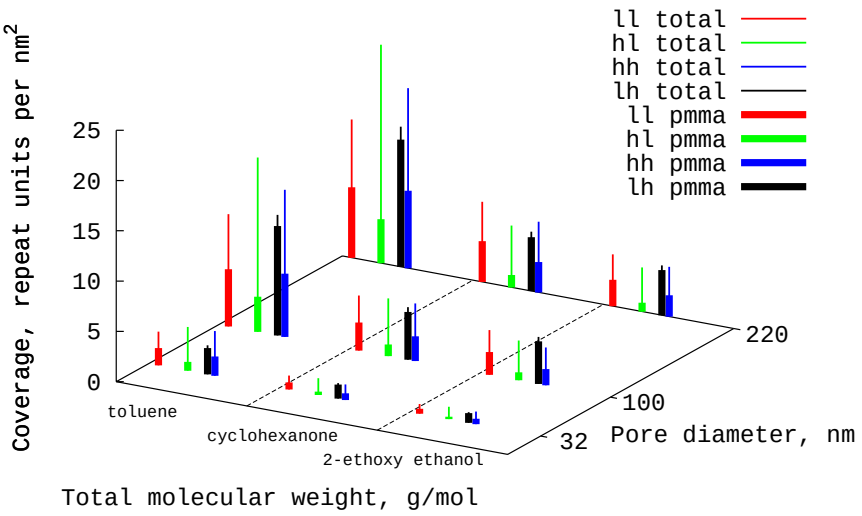

Figure 5.4: Effect of pore size, and solvent quality, and total molecular weight on coverage. The heavy lines represent MMA block adsorption, and the ultimate height of the lighter line is total adsorption. Therefore, it is acceptable to think of the heavy line as MMA block adsorption and the lighter line as PS block adsorption. The lighter+heavier = total (MMA+PS) adsorption.

(Figure 5.6). It is obvious from these plots that adsorption from toluene yields the most mass on the surface.

The reasons why these block copolymers do not behave similarly to homopolymer PMMA can be explained by adsorption mechanism, block asymmetry, and solvent quality. First I will discuss this result in light of the different mechanisms of adsorption of PS and PMMA to alumina. While PS forms weak and transitory interactions with the alumina surface by π bonding with the surface, (Figure reffig:psweak) PMMA is known to form stronger, direct bonds as previously explained and illustrated as Figure 4.1. Therefore, if we approach this problem from the viewpoint of de Gennes (anchor-bouy) model, PMMA is likely to make up the anchor, while PS the bouy. Let us assume that the PMMA block adsorbs to the surface in adsorption blobs, as proposed by Rubinstein [67], and that the PS block extends outward into the fluid as a buoy. This type of system can be illustrated in a one-dimensional system as Figure 5.7. It is obvious, therefore, that (if we fix the molecular weight of the PS block and assume that the size of the adsorption blobs does not change significantly with PMMA block molecular weight), an increase in the molecular weight of the PMMA block should lead to a *decrease* in the overall coverage, as shown pictorially in Figure 5.7. This result is in

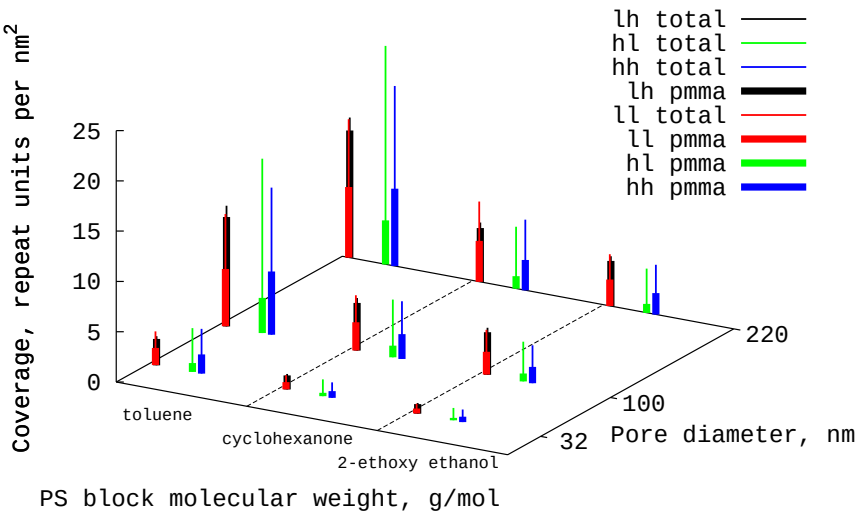

Figure 5.5: Effect of pore size, and solvent quality, and PS molecular weight on coverage. The heavy lines represent MMA block adsorption, and the ultimate height of the lighter line is total adsorption. Therefore, it's acceptable to think of the heavy line as MMA block adsorption and the lighter line as PS block adsorption. The lighter+heavier = total (MMA+PS) adsorption.

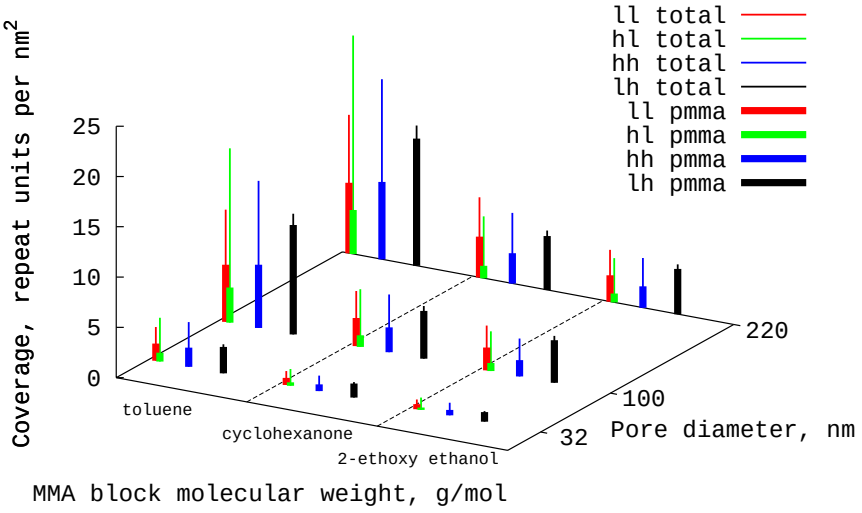

Figure 5.6: Effect of pore size, and solvent quality, and MMA molecular weight on coverage. The heavy lines represent MMA block adsorption, and the ultimate height of the lighter line is total adsorption. Therefore, it's acceptable to think of the heavy line as MMA block adsorption and the lighter line as PS block adsorption. The lighter+heavier = total (MMA+PS) adsorption.

opposition to homopolymer adsorption (Figure 4.3 and Figure 4.6), where adsorption increased with an increase in PMMA molecular weight up to a critical value, after which it remained constant. Such an occurrence as shown in Figure 5.7 would be evident in a plot of chain density *vs.* MMA block molecular weight. For these reasons, we expect chain density to decrease as MMA block molecular weight increases. This is generally what is shown in Figure 5.10. As MMA block molecular weight increases, chain density indeed decreases. Note that the same cannot be said for the PS block molecular weight (Figure 5.9) or total (PS+PMMA) molecular weight (Figure 5.8).

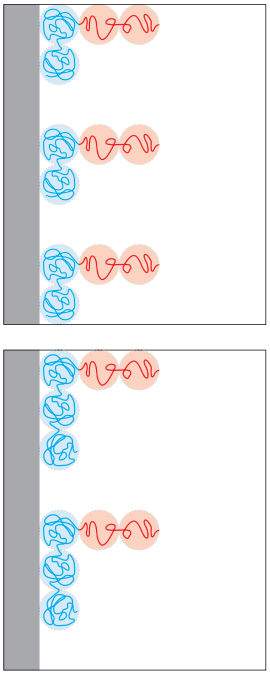

Figure 5.7: If the molecular weight of the buoy (red) block remains the same and the molecular weight of the anchor (blue) block increases, as it does from the upper image to the lower image, coverage is expected to *decrease*.

Let us now discuss the role of solvent quality on copolymer adsorption. The de Gennes anchor-buoy model assumes that one of the blocks is better-attracted to the surface than the other block. Therefore, phase segregation occurs, with one block close to the surface and another block extending outwardly, as shown in Figure 5.7. The framework with which we interpret this system is that solvent quality dictates how close reality is to this idealized de Gennes-Joanny model. In this particular system, a nonpolar solvent would lead to a more idealized anchor-buoy morphology because of the particular mechanism of adsorption. The PMMA block binds strongly and directly to the

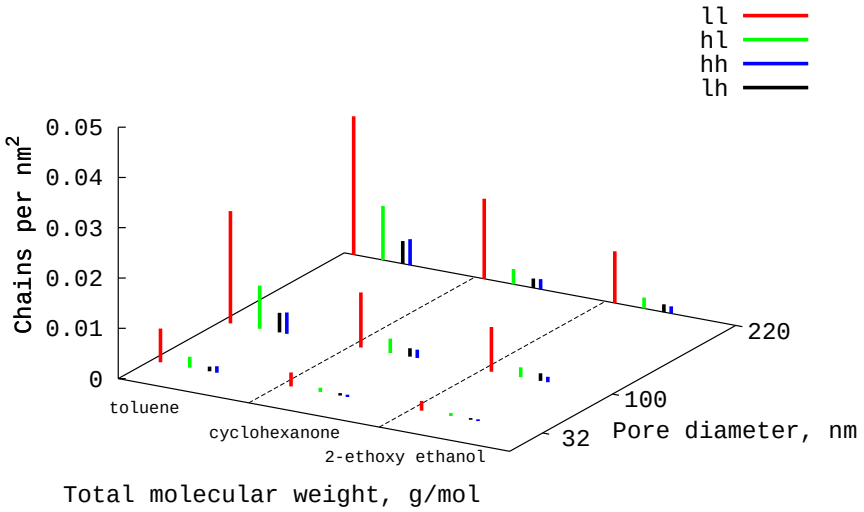

Figure 5.8: Effect of pore size, and solvent quality, and total molecular weight on *chain density*. Note the change in the z-axis from the previous plots. No heavy/light lines are required because each copolymer consists of one PS chain and one PMMA chain.

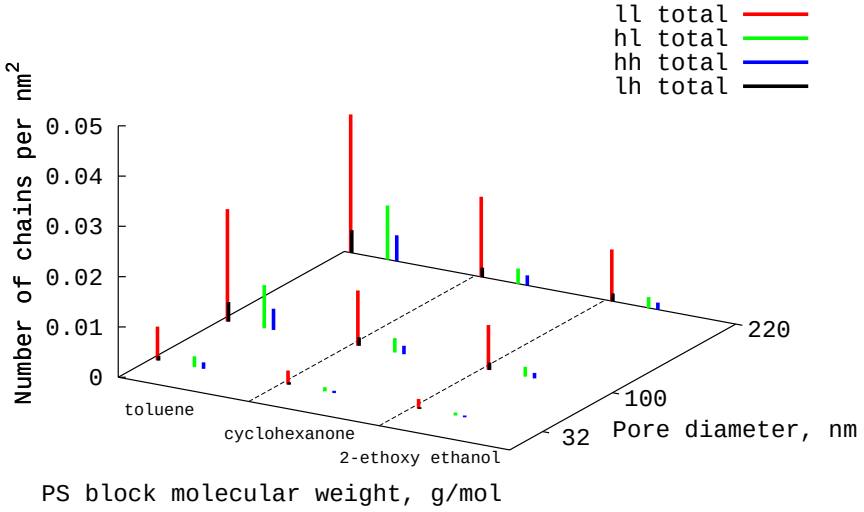

Figure 5.9: Effect of pore size, and solvent quality, and PS block molecular weight on *chain density*. No heavy/light lines are required because each copolymer consists of one PS chain and one PMMA chain.

4

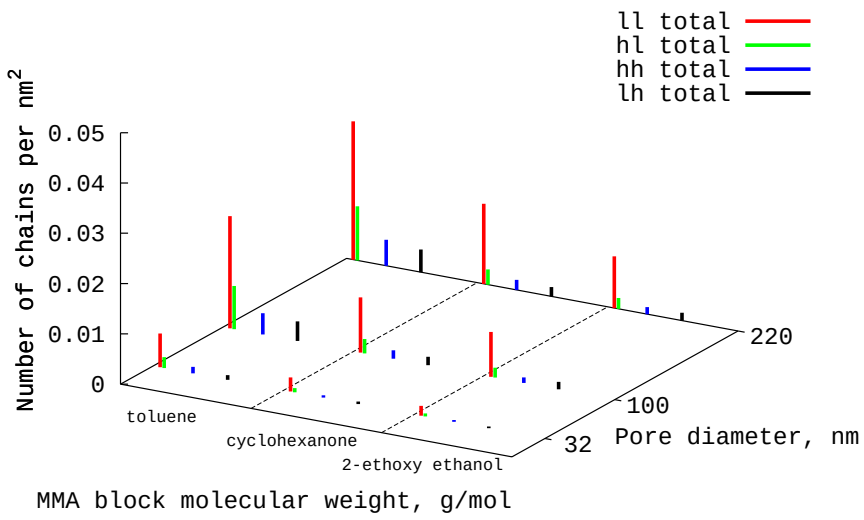

Figure 5.10: Effect of pore size and solvent quality, and MMA block molecular weight on *chain density*. No heavy/light lines are required because each copolymer consists of one PS chain and one PMMA chain. Notice the general trend and its relation to MMA molecular weight (as opposed to PS molecular weight, previous plot).

surface, while the PS block is weakly physisorbed (*vide supra*). Therefore, the PMMA block is a can be considered an anchor, while the PS block the buoy. This is especially true in a highly nonpolar solvent because the nonpolar block (polystyrene) extends outwardly into the good nonpolar solvent. Furthermore, the PS block must pay a much greater enthalpic penalty for leaving the good solvent for the surface. Therefore, the PS block is energetically discouraged from associating with the surface. All these reasons indicate that adsorption from a highly nonpolar solvent will lead to an idealized de Gennes-Joanny anchor-buoy system.

However, as the solvent becomes more polar (note the partial contributions ot the Hansen solubility parameter presented in Table 5.4. [86]), the system drifts from this idealization because the polystyrene block begins to associate with the surface. Its impetus, however, is solvent quality, as shown in Figure 5.11. When desorption occurs from a polar solvent, the PMMA block associates with the surface because of its strong affinity to the aluminum oxide, as described earlier. However, polystyrene *also* associates with the surface because it has a greater energetic incentive to avoid the solvent and instead associate with the surface. Therefore, what we have is no longer an anchor-buoy system but rather an anchor-anchor system, in which both blocks associate with the surface.

Table 5.2: Partial Contributions to Hansen solubility Parameter for Solvents Used in this Study

Solvent	δ_{polar} $MPa^{\frac{1}{2}}$	δ_{Hbond} $MPa^{\frac{1}{2}}$
2-ethoxy ethanol	1.4	2.0
cyclohexanone	6.3	5.1
toluene	9.2	14.3

It is easy to see that this anchor-anchor system would lead to lower values of both Γ and Ψ than an anchor-buoy system. And indeed this is what is observed experimentally. As solvent polarity increases (toluene–>cyclohexanone–>2-ethoxy ethanol), coverage and chain density both decrease noticeably.

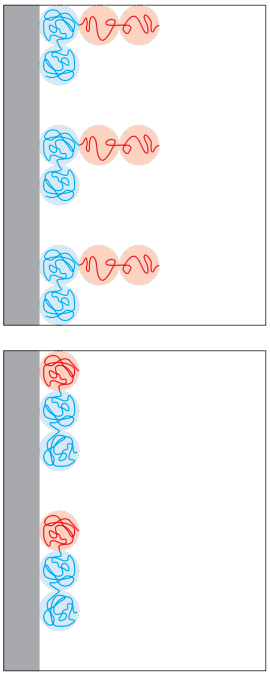

Figure 5.11: When adsorption occurs from a solvent that is good for the buoy block (toluene, in this case), the anchor-buoy model is adopoted (top). However, if the solvent is poor for the buoy block (2-ethoxy ethanol, in this case), the buoy block no longer behaves as a buoy and rather associates with the surface in order to escape the solvent (bottom). Such a rationalization explains the dependence of polymer adsorption on solvent.

As was observed previously for homopolymers, polymer coverage decreases significantly as pore size decreases. Surprisingly, relative block size and solvent choice do not significantly affect the magnitude or onset of this sharp decline. In the scope of this work, the the sharp dropoff in

copolymer coverage as curvature increases is an apparently unavoidable result.

5.5 Summary

Solvent quality, pore size, and block asymmetry all contribute to the extent of polymer coverage on curved surfaces. As the solvent becomes more polar, coverage decreases as a result of deviation from the ideal anchor-buoy model and an increase in the anchor block adsorption blob size. As the anchor block decreases in size, adsorption generally increases, as was shown also with the anchor-buoy model. Chain density was shown to increase as anchor block size decreased, as expected from the model. As observed in this system for homopolymers, block copolymer coverage was seen to decrease significantly as pore size decreases, and a simple geometric model was proposed to explain this phenomenon, as well as a similar phenomenon observed for adsorption to convex media (particles).

CHAPTER VI

GELATION OF CELLULOSE ESTER FLUIDS

6.1 Chapter Overview

The weak physical gelation of cellulose acetate propionate-butyl butyrate solutions as a result of the in-situ decomposition of iron pentacarbonyl complexes was explored. Viscometry and infrared spectroscopy were used to monitor the iron pentacarbonyl decomposition reaction progress and its effect on viscosity. Changes in viscosity in of the cellulosic fluids in general and gelation in particular were found to be dependent upon the environment in which the $Fe(CO)_5$ decompositions occurred. Systems under inert atmospheres exhibited a marked increase in viscosity, while systems under oxidative atmospheres exhibited a general *decrease* in viscosity. A hypothesis is proposed that explains the dependence of the viscosity of these cellulosic fluids as a function of the environmental conditions during the precursor decomposition. Under nitrogen atmospheres, zero-valent nanoparticles with highly reactive surfaces are synthesized, which form weak, transient bonds with the cellulosic polymer. The iron particles, under these circumstances, serve as weak bridges between adjacent polymer chains. Conversely, the primary particles synthesized under an oxidative atmosphere are metal oxides, which are less attractive to the polymer chain and, therefore, do not yield such bridges. This work demonstrates the capability to apply a simple method to control the viscosity of cellulose ester fluids.

6.2 Scope

Metal carbonyl complexes have attracted much attention in the nanomaterials literature because of their ability to form metal or metal oxide nanoparticles of narrow size distribution in polymeric media [18, 19, 21, 23, 24]. However, despite the extensive use of these complexes as metallic precursors, their ability to increase the viscosity of some polymer systems has been largely overlooked. Rolker and Glasner [87, 88] observed that the viscosity of ester-containing polymers was increased when they were treated with iron, cobalt, or nickel carbonyl complexes at elevated temperatures in

nitrogen. In this process, the metal carbonyls were assumed to behave as catalysts for increasing the degree of polymerization. Rolker's work emphasized only the impact of this high-temperature treatment on the polymer system, and the mechanism of this phenomenon has not been elucidated. Hence, one of the goals of this work is to determine whether the metal complexes behave as catalysts for covalent polymer-polymer bonding, as Rolker asserts, or whether their reactive decomposition generates products that associate with the polymer chains.

It will be shown that the thermal decomposition of $Fe(CO)_5$ in a cellulose acetate propionate-butyl butyrate fluid leads to an increase in viscosity, even up to the point of thermoreversible weak physical gel formation. This increase in viscosity will be shown to be a result of the interactions of the metal carbonyl decomposition intermediates and products with the polymer.

Cellulose acetate propionate (CAP) is a particularly interesting polymer in which to examine the influence of metal carbonyl complex thermal decomposition. It is a cellulose ester of the general formula shown in Figure 3.2 and a derivative of cellulose, a macromolecule that accounts for over half the carbon in the biosphere [29]. Rolker's work indicates that ester bonds are critical to the phenomenon described above [87, 88]; therefore, CAP, with its abundance of ester bonds along the polymer chain, is an appropriate candidate for this study.

In this study, the changes in the viscosity of cellulose acetate propionate-butyl butryate-iron pentacarbonyl systems were examined. Gelation was observed under specific conditions, and a framework was developed for the understanding of the underlying mechanism of this phenomenon.

6.3 Results and Discussion

The viscosity of the fluid was strongly dependent upon the environment in which the metal carbonyl decompositions occurred. Figure 6.1 shows the shear rate-dependent room-temperature viscosity of 7.6 mM $Fe(CO)_5$ in a 4.0% (w/v) CAP-butyl butyrate system bubbled with oxygen (a) and nitrogen (b) at 150 ^{o}C as a function of $Fe(CO)_5$ reaction time. The room-temperature viscosity of the former system decreased considerably as a function of time, while the viscosity of the latter system increased significantly. The latter system formed a gel at room-temperature after about two hours of reaction of the $Fe(CO)_5$, and the viscosity of the former system approached that of pure solvent after the same amount of time at room temperature.

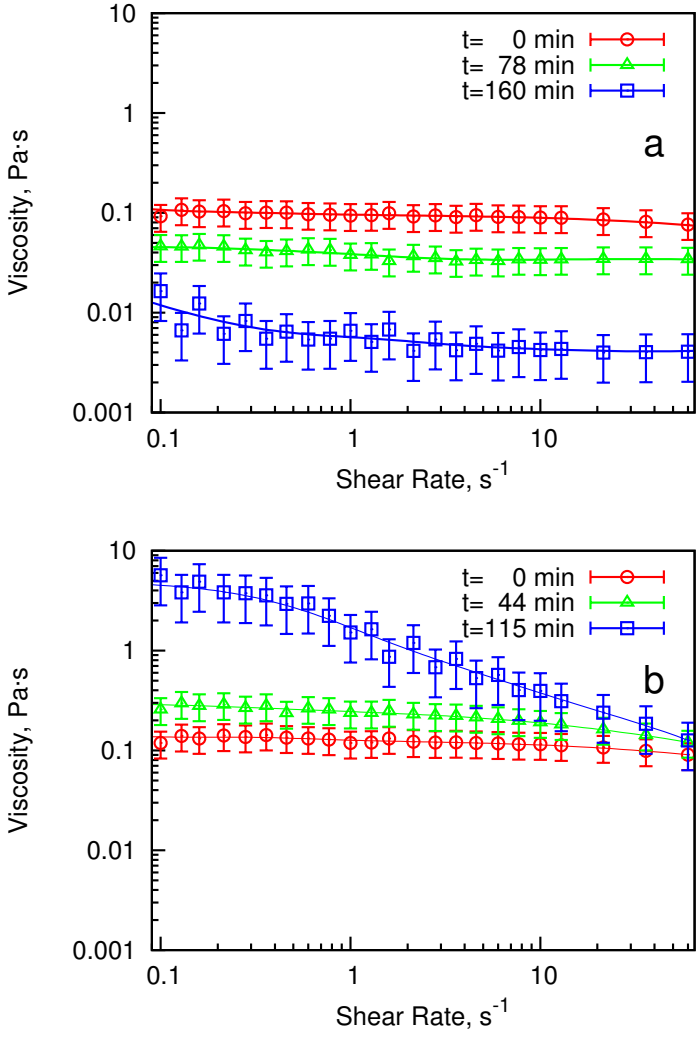

Figure 6.1: a) Room-temperature viscosity of the oxygenated CAP-butyl butyrate-$Fe(CO)_5$ system. The viscosity decreased significantly over time. b) Room-temperature viscosity of the nitrogenated CAP-butyl butyrate-$Fe(CO)_5$ system. The viscosity increased significantly for two hours of $Fe(CO)_5$ thermolysis, after which a room-temperature gel was observed.

The dependence of the viscosity of these systems on the environmental conditions under which the decomposition was conducted is shown in Figure 6.2, which shows the room-temperature viscosity at a fixed shear rate, arbitrarily chosen as 10 s^{-1}, along with $Fe(CO)_5$ concentration as determined by the disappearance of the carbonyl absorption bands at 2021 and 1996 cm^{-1}, corresponding to the singly degenerate out-of-phase motion of the axial carbonyls with A2" symmetry (axial stretching mode) and to the doubly degenerate motion of the equatorial carbonyls with E' symmetry (equatorial mode), respectively [89–94] as a function of decomposition reaction time, as shown in Figure 6.3.

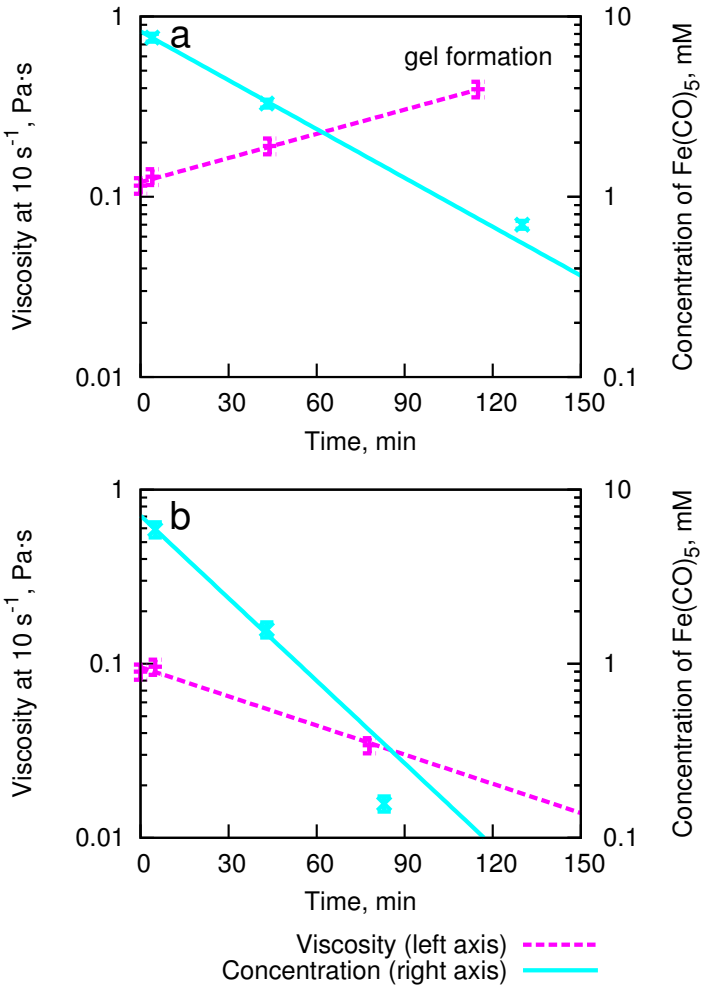

Figure 6.2: Room-temperature viscosity and $Fe(CO)_5$ concentration of a) the nitrogenated CAP-butyl butyrate-$Fe(CO)_5$ system and b) the oxygenated CAP-butyl butyrate-$Fe(CO)_5$ system as a function of time. The lines represent best-fit first order kinetics.

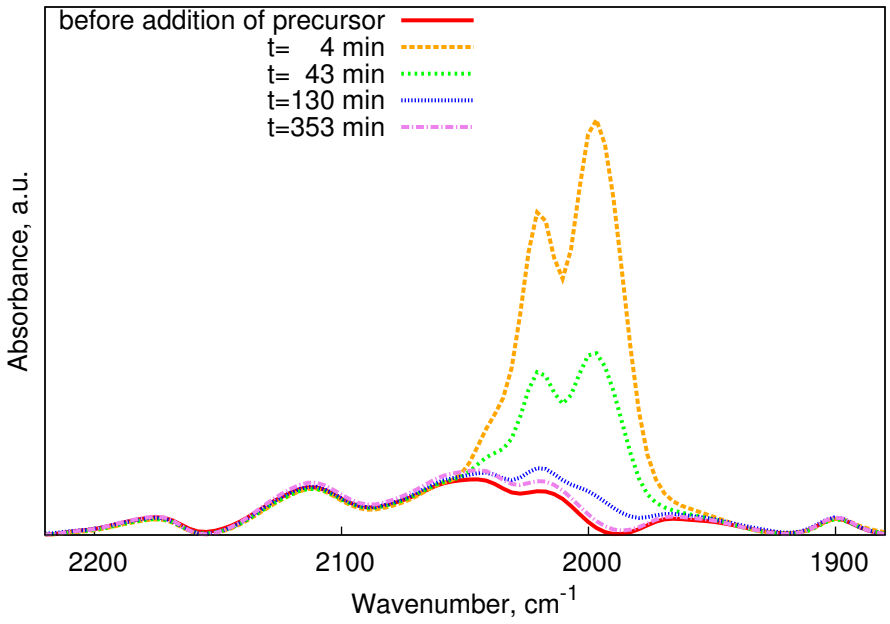

Figure 6.3: Infrared spectra of the $Fe(CO)_5$-CAP-butyl butyrate system before (*i.e.* t=0 min) and during reaction. $Fe(CO)_5$ concentrations in Figure 6.2 were determined spectroscopically by the absorbance of the carbonyl peaks around 2000 $cm^{-}1$ after normalization *via* Beer's Law.

The $Fe(CO)_5$ concentration-viscosity-time plots for both the system under a nitrogen atmosphere (Figure 6.2 a) and the system under an oxygen atmosphere (Figure 6.2 b) reveal opposing correlations between decomposition reaction kinetics and the viscosities of these systems. The decomposition reaction of the metal carbonyl precursor occurred faster in oxygen. In oxygen, the reaction was 95 % complete at approximately 60 minutes, while the reaction was 95 % complete in nitrogen at about 90 minutes. This discrepancy in reaction rate is most likely due to additional reaction pathways that were not possible in inert atmosphere. Under these conditions, $Fe(CO)_5$ (or, most likely, one of its highly reactive derivatives) was able to react directly with elemental oxygen to form an oxide [95, 96].

Unlike the decomposition reaction rates that show the same general behavior for both the oxygen and inert environments (albeit the modestly different rates), the viscosities in both systems exhibit opposing behavior as a function of reaction time. The decrease in viscosity in the oxygenated system can be understood after performing a control experiment in the absence of $Fe(CO)_5$. A 4.0% CAP-butyl butyrate system showed a similar decrease in room-temperature viscosity when heated at 150 ^{o}C over the same time period, possibly due to the significant polymer scission that may occur

under these conditions. This likely depolymerization is peripheral to this work; however, I shall speculate about its mechanism briefly. Glycosidic bonds are quite susceptible to oxidative cleavage under acidic and basic conditions [97], which could exist after ester hydrolysis along the polymer chain around 150 ^{o} C [98].

Hence, the decrease in polymer molecular weight that is responsible for the decrease in viscosity for both the $Fe(CO)_5$-containing polymer solution and the $Fe(CO)_5$-free polymer solution (Figures 6.1 a and 6.2 b) is most likely caused by the thermal treatment. Conversely, the viscosity of a similar control solution placed under nitrogen remained unchanged. Moreover, the room-temperature viscosity of a $Fe(CO)_5$-CAP-butyl butyrate solution increased and eventually led to weak physical gelation.

While the decrease in the viscosity of the oxygenated system is easily explained, the reasons for the increase in viscosity and subsequent gelation of the Fe(CO)5-CAP-butyl butyrate solution that was placed under a nitrogen atmosphere are less obvious. In order to explain the increase in room-temperature viscosity and subsequent gelation of the nitrogenated $Fe(CO)_5$-CAP-butyl butyrate system, it was compared to the control for which the viscosity remained unchanged. Therefore, it can be concluded that the increase in viscosity and subsequent onset of gelation was somehow related to the presence of the $Fe(CO)_5$ in the system.

The explanation that is proposed here (Figure 6.4) is that the reactive, zero-valent species that are formed during the decomposition of $Fe(CO)_5$ (such as Fe^0) associate with the polymer chain. Because the reaction products are known to exist as clusters [18, 19, 21, 23, 24], shown here in Figure 6.5, each cluster can be expected to associate with several different polymer chains, thereby promoting the formation of a weak physical gel.

I will now justify and clarify the designation of the fully reacted, nitrogenated system as a weak physical gel. In this work, I invoke the broad definition of gelation described by Rubinstein [67] and Ferry [99], rather than the more rigid criterion described by Winter and Chambon [100]. Without perturbation or temperature elevation, the weak gel is not observed to flow over months of storage, which satisfies the broad criteria of Rubinstein and Ferry (namely that the material is substantially diluted and exhibits no steady state flow on specific time scales). Furthermore, experimental evidence indicates that the bonding between polymer and particle is weak and transient, as has been

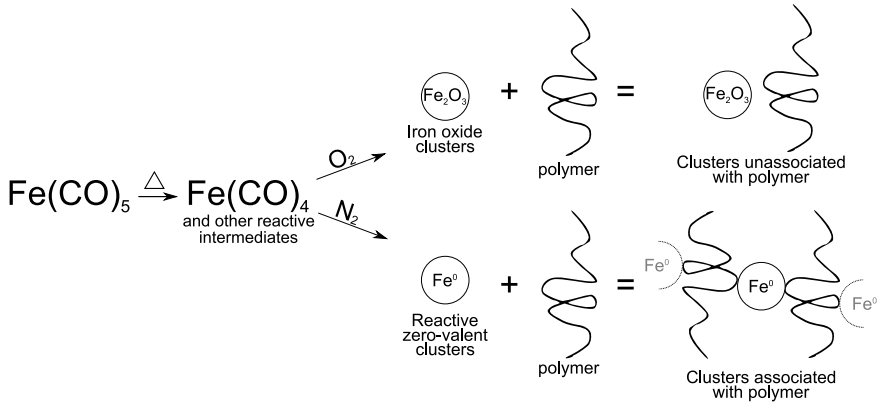

Figure 6.4: The general explanation for the occurrence for the phenomenon reported in this work. In nitrogen, the zero-valent nanoparticles that result from the thermal decomposition of $Fe(CO)_5$ interact with the polymer. However, in oxygen, these nanoparticles are fully oxidized and cannot interact with the polymer.

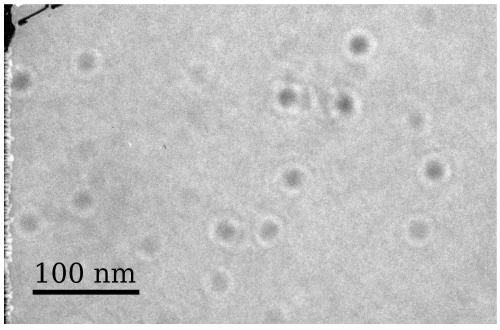

Figure 6.5: Particles synthesized by the thermal decomposition of $Fe(CO)_5$ in the nitrogenated CAP-butyl butyrate system. The black scale bar represents 100 nm.

shown by three separate experiments. 1) The weak gel formed in the nitrogen atmosphere pathway shown in Figure 6.4 is a thermal (reversible) gel, rather than a chemical (covalent) gel. The increase of its temperature to approximately 90 ^{o}C will yield a transformation from a weak gel to a liquid; 2) The gel can be mostly dissolved in excess acetone, which is an excellent solvent for CAP. The centrifugation of this CAP/Fe gel-butyl butyrate-acetone system yields an off-white, opaque precipitate. However, this precipitate is a minor component and does not affect the gelation. After the acetone (but not residual butyl butyrate) is driven off from the supernatant and the supernatant is cooled, a weak gel is formed once again. The affinity of acetone to the polymer enhances polymer-solvent interaction and diminishes polymer-particle interaction. Conversely, butyl butyrate is a much poorer solvent, and hence, polymer-solvent interactions are inhibited; 3) The viscosity of the gel decreases dramatically at high shear rates, as seen in Figure 6.1 b. Such behavior indicates the breakdown of the weak gel with sufficient stress. Because the gel can be destroyed and re-formed by variation in temperature, solvent, and shear stress, it can be inferred that the bonding between particle and polymer is weak and transient.

I will now further develop and justify this hypothesis in relation to the literature published on the subject. $Fe(CO)_5$ is known to decompose via a cascade mechanism in which discrete CO ligands dissociate from the metal core, *i.e.* [101–105] as shown in Equation 6.1.

$$Fe(CO)_5 \rightarrow [Fe(CO)_4] + CO \rightarrow [Fe(CO)_3] + 2CO \rightarrow \ldots Fe + 5CO \tag{6.1}$$

The intermediates and products shown in Equation 6.1 are both highly reactive and zero-valent. Hence, the specific intermediates shown in Equation 6.1 may be observed in the infrared only in the gas phase, at extremely low pressures, and at short time scales (in order to limit molecular collisions and, therefore, further reaction) [104]. It is not surprising, therefore, that these species react even more readily in the condensed phase, where such reactions can occur on the order of picoseconds, as reported by Welch *et al.* [106]. It is expected, therefore, that the metal cluster products of $Fe(CO)_5$ decomposition in nitrogen will associate with the polymer chains for the same reasons that iron readily forms oxides or hydroxides when exposed to air or water.

These accounts support the hypothesis, *i.e.* that these zero-valent species form weak bonds with the polymer chain. The specific chemical group of the polymer that bonds with the iron, however,

is unclear. Infrared and Raman spectra showed no new peaks in this study. Literature reports [107–113] have determined that Fe^0 from $Fe(CO)_5$ decomposition interacts with OH groups, as shown in Equation 6.2. This explanation is further supported by Kurokawa *et al.*, who observed this type of bonding in cellulose ester-metal alkoxide systems [114,115]. Furthermore, other researchers report the presence of hydrogen bonding between metal carbonyl decomposition and alcohol groups in cellulose derivatives [116]. Recall that the chemical structure of the CAP polymer implies that there is an abundance of OH groups along the polymer chain.

$$Fe_x(CO)_y + \rangle CAP\text{-}OH \longrightarrow [(\mu\text{-}H)Fe_x(CO)_{y-2}\{\mu\text{-}OCAP\langle\}] + 2CO \tag{6.2}$$

In addition to the OH groups, there is also an abundance of COOR groups, and these can also associate with zero-valent iron particles [116]. Moreover, the observations of Rolker *et al* [87, 88] regarding the increase of the viscosity of ester-containing polymers in the presence of some transition metal carbonyls at elevated temperatures imply that ester group in the polymer is necessary for inducing the occurrence of such a process. This suggests the formation of a weak Fe-COOR bond, where the inorganic species serve as weakly bonded bridges between polymer chains thereby promoting a rise in viscosity. This is supported by Buser and Heidinger [117], who reported resin hardening by the mixture of metal ions (specifically, Pb^{2+} and Mn^{2+}) with polyesters. Of course, in the presence of oxygen during the decomposition reaction (as discussed in the previous section), the zero-valent metallic species are oxidized by the available oxygen [95, 96] and are therefore unable to associate with the polymer. This hypothesis explains the fact that weak physical gelation occurs only in nitrogenated systems.

To test whether this hypothesis is correct, different metal carbonyl precursors were used whose thermolysis products would exhibit different affinities toward the polymer. For example, we would expect the thermal decomposition of the carbonyl complex of a noble metal, such as $Ru_3(CO)_{12}$, to impart no significant changes to solution viscosity in this system under nitrogen because the reaction products of Ru would have a considerably lower attraction to the polymer. (The electrochemical half reaction $Ru = Ru^{++} + 2e^-$ has a standard electrode potential of +0.455 V SHE [118].) Conversely, an oxide-forming metal carbonyl similar to $Fe(CO)_5$, such as $Co_2(CO)_8$ would be expected to exhibit similar behavior, leading to the onset of weak physical gelation in this system under nitrogen. (The

half-reaction $Co=Co^{++} + 2e^-$ has a standard electrode potential of -0.277 V SHE (*cf.* $Fe=Fe^{++} + 2e^-$, -0.440 V SHE).) Indeed, the experimental data are in good agreement with hypothetical predictions, as can be seen in Figure 6.6. The Ru-based system shows no significant changes in viscosity, while the Co-based system eventually forms a gel, as predicted.

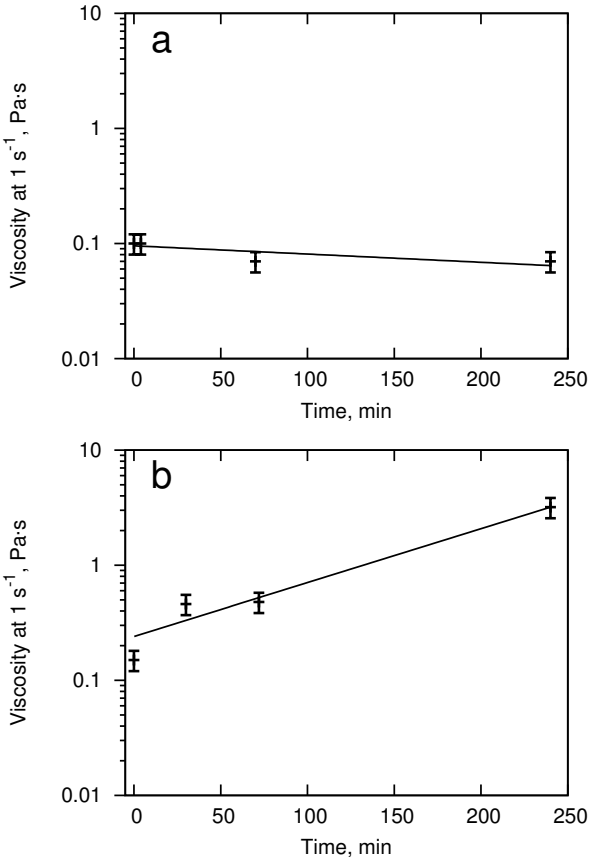

Figure 6.6: Room-temperature viscosity of the nitrogenated $Ru_3(CO)_{12}$ system (a) and $Co_2(CO)_8$ (b) as a function of time. The hypothesis predicts that decomposing a noble metal carbonyl will not significantly affect the viscosity of the system and that decomposing an oxide-forming metal carbonyl will lead to an increase in viscosity. These predictions are accurate. The solid black lines represent best-fit first order kinetics.

This method of viscosity control is particularly relevant because a traditional limitation of cellulose esters is the severe molecular weight loss due to processing. The molecular weight of some native cellulose fibers may be greater than 10^6 g/mol. However, after processing and esterification, the resultant molecular weights may be less than one tenth of the original value [31]. Therefore, the method of using iron particles to control the viscosity of cellulose esters is valuable because it enables the discerning scientist to impart properties consistent with longer molecular weight polymers,

such as increased viscosity, if such properties are desired.

6.4 Summary

In this work, the decomposition of $Fe(CO)_5$ in the CAP-butyl butyrate system in nitrogen leads to an increase in viscosity, followed by the onset of gelation, while the viscosity of the same system in oxygen decreases significantly. The decrease in viscosity under oxygen was shown to be a result of the oxidative degradation of the polymer chain at elevated temperatures irrespective of the presence of $Fe(CO)_5$ in the system. However, the increase in viscosity of the system under nitrogen was determined to be a direct consequence of the presence of $Fe(CO)_5$ thermolysis products in the system. The intermediates and products generated by the thermal decomposition of reactive metal carbonyl precursors associate with the polymer, which leads to weak bonding between iron particles and the polymer chains. However, if the decomposition products are inactive (*e.g.*, if they are noble or metal oxides), these associations cannot occur, and no significant viscosity change is observed. Ruthenium and cobalt carbonyl complexes were used, which differ in their reactivity (Co a base metal and Ru noble), in order to test this hypothesis. The results showed that the less reactive metallic species embedded in the CAP-butyl butyrate system (Ru) were in fact unreactive and did not associate with the polymer, while the more reactive metallic species (Co) gave rise to gelation, in good agreement with the predictions of the hypothesis. This work is significant because it shows a simple, economical way to control the viscosity of cellulose ester fluids.

CHAPTER VII

FUTURE WORK

7.1 Chapter Overview

Future steps that are likely to advance the current work are discussed. Additional experiments are proposed, including economically feasible methods for synthesizing alumina substrates with controllable pore geometry, which will facilitate the numerous and substrate-intensive experiments described. An exploration of the mechanical properties of formed nanocomposites is proposed.

7.2 Experiment Suggestions

In addition to the proposed future work for polymer and copolymer adsorption to curved surfaces, possible future work for cellulosic nanocomposites is presented here. It stands to reason that larger molecular weight CAPs would require fewer crosslinking bridges in order to form a gel. This is a testable hypothesis because additional molecular weights of CAP can be acquired and tested. Care would have to be taken to account for differences in particle size, which may arise as a result of a variation in polymer molecular weight. [23]

Furthermore, the mechanical properties (of the gel and of resultant xerogels and aerogels) and their correlation to experimental parameters is a possible next step in this work. Because of the interactive nature of the particles to the polymer, we can expect dried composite films formed by this method to be stronger than unfilled polymer. The dependence of breaking strength on precursor (and, therefore, filler) concentration would indeed be an interesting study.

Additional cellulosic esters, such as cellulose acetate and cellulose acetate butyrate, could be investigated to determine the applicability of this method and to what extent polymer-polymer interactions [119, 120] facilitate this phenomenon.

Additional experimental work may elucidate the curvature-dependent adsorption of polymers and block copolymers to curved surfaces. The present work has presented attempted to show how

many chains adhere to the inorganic surface. However, the additional parameters of anchor density and adsorbed layer thickness are also important because together they can provide an accurate depiction of polymer conformation at the surface. Key examples are the Silberberg and the Simha-Frisch-Eirich theories, [66] which allow for the determination of the bond energy between repeat unit and surface from polymer molecular weight, thickness, anchor density, and adsorption isotherm.

Previous researchers have determined anchor density in the PMMA-alumina system by measuring the relative intensities of the C=O stretching modes at 1740 and 1690 cm^{-1}. Such measurements were unable to be performed in this work because of low signal intensity of these C=O vibrations in transmission and attenuated total reflection FTIR. It is hypothesized here that, diffuse reflectance may provide enough signal for this technique to be appropriate. Transmission FTIR fails for two reasons: 1) the alumina absorbs infrared radiation and 2) the mass of polymer or copolymer in the path of the beam is quite small (Given the spot size, I have estimated this mass to be less than 0.02 mg). Attenuated total reflection fails also because the interaction volume is limited. However, diffuse reflectance, in which infrared radiation would interact with the adsorbed polymer layer, reflect in multiple directions, and then be focused back into the detector, might provide enough intensity to measure PMMA adsorption in this manner.

Because anchor density, coverage, and layer thickness are inter-related, thickness can be measured to infer anchor density, given coverage. A method of thickness measurement has been implemented in a similar system. It applies the principle of Poiseuille flow, in which the pressure drop across a cylinder is related to the radius of said cylinder according to the following equation:

$$\frac{\Delta P = 8\mu L Q}{\pi r^4} \tag{7.1}$$

A representative alumina membrane studied in this work can be approximated as an array of cylinders. Therefore, assuming the boundary conditions do not change as the adsorbed layer grows, the thickness of said layer can be calculated by measuring the pressure drop across the membrane.

Another interesting parameter to measure would be kinetics. In the present work, an attempt has been made to determine the sufficient duration of exposure to solution in order to achieve equilibrium conditions. A representative plot using this technique is Figure 4.2, which was used to infer the

kinetics of the system. However, a higher resolution plot would be interesting in order to compare adsorption to alumina nanostructures of different nanoscale dimensions. Such resolution could be achieved by the previous (Poiseuille) method. Another, more common, technique is the analysis of the solution for a change in concentration. Or a sensitive balance as described in the first chapter of *Adsorption of Polymers* by Lipatov. Intrinsic viscosity. [66]

Given such a system, I present some hypotheses that could confirm some of the main points of this dissertation. First, for adsorption of PS-b-PMMA copolymer to alumina should occur in a two-step process because of the differing mechanisms of adsorption of the two different blocks as described in Chapter 5. After initial saturation of block copolymers at the alumina surface, PMMA should slowly displace PS on the surface, which should lead to a thicker adsorbed layer (if already-adsorbed MMA blocks displace PS blocks), more mass adsorbed (if new chains displace PS blocks), or both. Solvent quality, molecular weight, and block asymmetry are expected to influence these kinetics.

Yet another interesting thing to look at would be whether chains of a particular molecular weight adsorb preferentially to the surfaces. A representative approach in the literature describes such analysis of humic acid solutions before and after adsorption to activated carbon by gel permeation chromatography. [121] The initial hump is obtained, and what's missing from it later is analyzed.

Adsorption isotherms that plot coverage (or a comparable term) *vs.* solution concentration are quite revealing. A typical plot of an adsorption isotherm is shown as Figure 7.1. Note that although Figure 7.1 looks similar to Figure 4.8, the *x* axes are quite different. Data like those shown in in 4.8 are calculated from *only one concentration*. Proper adsorption isotherms for the concave alumina studied in this work can only be calculated after data collection for many, many concentrations. Typical experimental works measure at least ten concentrations.

Many of these experimental suggestions will require a mass of porous aluminum oxide of a magnitude much greater than that explored in this work. Because of the sensitivity of the TGA balance, only fractions of a milligram of polymer needed to be adsorbed to a substrate that would fit into the TGA pan. However, in order to measure real-time adsorption kinetics by infrared spectroscopy, as proposed previously in this chapter, enough polymer must be adsorbed in order to evince a measurable change in solution concentration. Due to the sensitivity of the spectrometer in our laboratory,

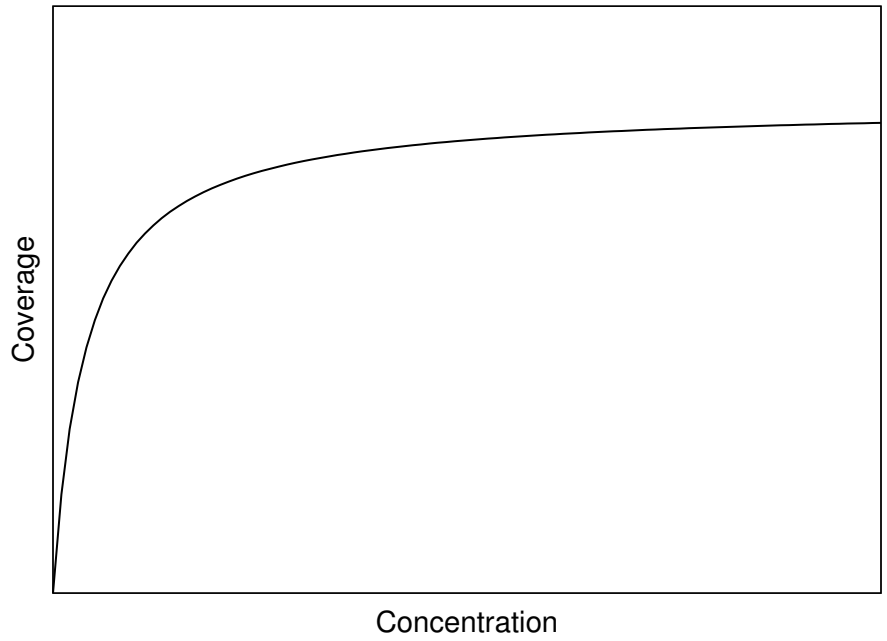

Figure 7.1: A Langmuir isotherm, so named for its champion, Irving Langmuir.

I have estimated that the minimum amount of substrate required for one such kinetics experiment would be 1 g. The primary reason that a small mass of alumina was used in this work is cost. The anodic aluminum oxide used in this work was purchased directly from Whatman at a considerable cost of approximately $ US 1.50 per disc. Because each disc has a mass of approximately 15 mg, one kinetics study would require on the order of 100 discs. If performed in triplicate for statistical meaningfulness and with variation of the most critical experimental parameters, such as polymer or copolymer molecular weight and pore size, it is easy to see how the budget *for substrates only* for such a simple experiment would approach and possibly exceed the cost of the measurement tools used to collect the data. If adsorption isotherms are to be collected, multiple concentrations must also be explored, which is expected to increase the substrate cost by an order of magnitude.

7.3 Engineering of Anodic Aluminum Oxide

It is expected that the cost of these alumina substrates could be considerably decreased if they were synthesized on-demand in the laboratory. However, these anodic aluminum substrates need not be purchased from a vendor. Rather, they can be synthesized in the laboratory by a relatively simple anodization process. Some empirical relationships have been determined that relate experimental

parameters to pore geometry, and these are of utility to the practical scientist. Among the simplest and most universal of these relationships is the apparent linear relationship between anodization potential and pore diameter. Depending on the electrolyte, this dependence generally lies between 1-3 nm/V, as applied voltage increases from top-to-bottom. [122–125] Additionally, penetration depth appears to vary linearly with the duration of anodizing. [123] Other empirical relations are discussed in the literature, and some will be highlighted here. Because the mechanism of pore formation is so poorly understood, each parameter reported here must be considered an isolated example, as other reports sometimes present contradictory data. An increase in $[H^+]$ (*i.e.* a decrease in pH) makes oxide dissolution more energetically favorable. As a result, the pore grows into the metal surface faster, requiring less cross-sectional area (*i.e.* a smaller pore diameter) to satisfy Faraday's law. [126] Temperature of anodization was shown to influence the pore size but not in any predictable fashion. [127] Great experimental inconsistencies exist, with one report indicating a decrease in porosity with increasing potential in a sulfuric acid system and another indicating an increase in porosity with increasing potential in a sulfuric acid system. The dependence of porosity on temperature gives similarly contradictory results. [122] The lesson to take from these relationships (or non-relationships) is that they aren't well-understood.

Because anodic films typically exhibit uniform and uniformly distributed pores (Chapter 2), they are ideal candidates for nanofabrication. This application is in contrast to the primary industrial applications of protection and decoration in that, for nanoscience, the surface is what is important. As far as typical anodizing goes, what's important is the bulk - how it looks and how well it retains its mass and structural integrity over time. Therefore, the first practical aspect of anodizing for nanofabrication is how to get rid of the what's below the oxide layer, a concept that would seem counterproductive to most corrosion scientists. Primitively, as in the case of O'Sullivan, [125] the surface film is removed from the aluminum by literal brute force, prying it from the metallic surface. More elegant techniques can be used, such as dissolution of the residual aluminum with $HgCl_2$, followed by treatment with phosphoric acid to remove the barrier layer. [123] More primitive methods may be used also, such as the peeling of the layer with nail polish. [128] Yet another likely possibility is the use of the surface as a template, which will be discussed below. [125] What seems obvious but that hasn't been reported is the complete anodization of a thin aluminum foil, which

would preclude the (highly dangerous) step of $HgCl_2$ treatment.

Anodic aluminum oxide may be used as a mold for other materials for many applications. For example, the porous layer can be filled with molten thermoplastic polymer, which can then be cooled and separated from the surface in order to achieve an array of polymeric pillars. This pillared structure, too, can be used as a mold for other materials. In this application, another material, such as platinum, is deposited onto the pillared structure.

The applications of anodized aluminum oxide structures to nanotechnology are abundant, due to the regularity and controllability that the process affords. Anodic aluminum oxide may be used as a mold for other materials for many applications. For example, the porous layer can be filled with molten thermoplastic polymer, which can then be cooled and separated from the surface in order to achieve an array of polymeric pillars. This pillared structure, too, can be used as a mold for other materials. In this application, another material, such as platinum, is deposited onto the pillared structure. The result is a new material *of identical geometry to the original alumina*. Consequently, ordered porous structures with properties that are radically different from the original alumina may be formed. This process is expected to be useful for ordered porous media in which the properties of alumina (its brittleness and poor electrical conductivity, *e.g.*) are undesirable. A related application is the use of anodized aluminum oxide as a mask for the manufacture of other materials. For example, a regular array of gold nanodots may be deposited through open-ended nanoporous alumina onto a substrate. [122, 123]

In addition to the typical experimental parameters that may be varied to control pore size and pore geometry, additional techniques may be used to control the shape, size, size distribution, and order of the pores formed by anodizing aluminum. It is important to note that these methods are much more predictable than control via voltage and acidity, which are described above. The ideal pore structure was presented as a regularly ordered three-dimensional network of aligned cells. However, in practice, the network is rarely as perfect as in the ideal case. The discerning materials scientist will notice some typical defects: grain boundaries, edge dislocations, and point defects. Superior regularity may be achieved by three different ways.

First, the duration of anodizing plays a role on regularity. The order of the system is greatly improved as exposure time increases. As the pores advance into the substrate, the advancing front

becomes more ordered. This tendency that can be exploited in order to achieve regular pore structure throughout a film. This three-step process involves allowing anodizing to proceed until this regular advancing front is achieved, then etching away the original, randomly oriented, superficial pores, then continuing anodizing. The entire porous layer is regularly structured after the entire process. [123]

A final, extremely versatile, method of achieving regularity, is the prepatterning of the surface so that pore growth proceeds only at desired locations. Depending on the arrangement of the indentations, unnatural pore geometries may be achieved. Prismatic (rather than cylindrical) pores can be formed by an unnatural arrangement of pore initiation sites. [123] And what this means is that polymer and copolymer adsorption can occurr not only in cylidrical pores but also pores of many different geometries.

Because the regularity of this oxide layer can be promoted, modified, and exploited with a wide variety of techniques, it yields well-defined and controllable pore geometries and sizes and is valuable to the work presented in the present document.

CHAPTER VIII

CONCLUSIONS

The main conclusions of this work are 1) curvature need not be extreme in order to observe nanoscale effects and 2) a surprisingly small amount of particle loading in cellulosic nanocomposites can have profound effects on composite properties.

One of the most surprising results of this work is that the adsorption of polymers to pores decreases significantly at what some would consider near-nano pore sizes. A pictorial explanation of this surprising result is shown in Figure 8.1, [129, 130] which shows two well-known nanoscale effects (melting point decrease and band gap increase) along with polymer adsorption investigated in this work. Melting point depression and band gap increases occur only for very small particles. A decrease in particle radius from 100 to 50 nm evinces a barely noticeable decrease in melting point (about 22 K), and the change in band gap as a result of such a shrinking is practically nonexistent (10^{-7} %). The change in polymer adsorption, however, is quite noticeable.

A recent trend in the literature denotes the 50 nm radius range as somehow insufficiently nano-sized. Much value has been attached to this particular prefix, leading to concern over which products should be marketed as *nano* and what research should be funded under its umbrella. [131–134] However, the data, which are indifferent to such matters, show that a decrease in pore diameter from 200 nm to 100 nm diameter has a profound effect on polymer adsorption to such pores, nearly halving polymeric coverage. A similarly profound result is shown for polymer adsorption to particles of similar sizes. [40–42] It is postulated here that the primary reason for such a difference in what would be considered modest curvatures is the length scale of the adsorbate. Much smaller adsorbates would likely not adsorb differently to these two different pore sizes, and this is the operating principle of Brunauer-Emmett-Teller surface analysis by gas adsorption. [135] As another example, small-molecule thiols often used in self-assembled monolayers, to undergo a 2-times difference in coverage over gold, the particle size must effectively decrease from flat to about 1 nm radius. (Interestingly, for reasons beyond the scope of this work, the coverage actually *increases* in the thiol-gold

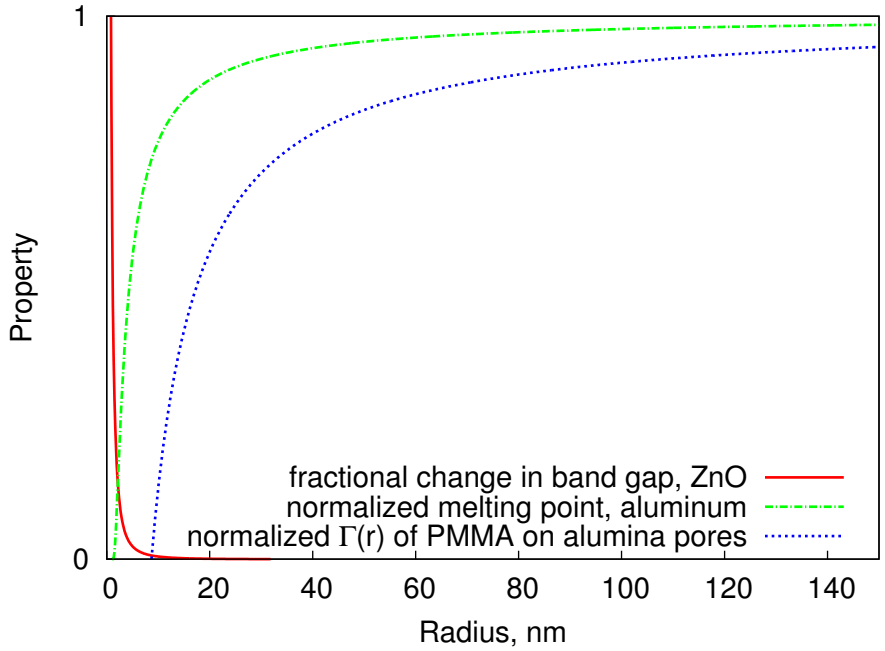

Figure 8.1: Selected properties with respect to particle or pore radius. Fractional change in zinc oxide band gap (Eg=3.44 eV) , melting point of aluminum divided by its bulk melting point (933 K)), and adsorption of PMMA to alumina divided by its bulk maximum (model from this work).

system as particle size decreases. [136, 137]) In comparison to elemental nitrogen and low molecular weight thiols, polymer chains are quite large. Typical root-mean-square end-to-end distances of a freely rotating polymer chain are 1-10 nm. [67] A low molecular weight thiol, such as those reported in Li [137], would have an end-to-end distance in the 2 Å range. It is easy to see, therefore, long polymer chains would be more affected by near-nano constriction than small molecules.

Yet another profound implication of the work presented in this document is the relatively small amount of nanoscale particulate filler that must be added to significantly modify composite properties. Consider, for example, the nanocomposites presented in Chapter 6. Only 0.1 volume percent of nanoscale filler was required to transform a fluid into a physical gel. Commensurate zero-shear viscosity increases (of approximately 2 orders of magnitude) have been achieved with nanocomposites in the literature of of 6 wt% clay in polypropylene, [138]. More modest changes (approximately one order of magnitude) in viscosity have been observed for similar nanocomposite systems. [139, 140] Such profound changes are generally unthinkable in the realm of typical composites. For example, typical (macro)composite suspension viscosity models, such as the Einstein prediction ([141] and

pertinent references therein) allow for such profound changes to occur only at extremely high volume fractions of filler, and this limitation of macrocomposites is observed in many experimental studies. [142–144] It is proposed here that the large specific surface area of nanoparticles (Figure 1.1), their attraction to the cellulosic polymer (Chapter 6), and the extreme affinity that cellulose acetates have for one another even in dilute solutions and in good solvents [119, 120] all contribute to the extreme property change as a result of the inclusion of nanoparticles in polymeric media.

This work presented a study on nanocomposites, including at which point do polymer chains begin to adsorb differently onto curved media as opposed to flat media. Furthermore, a particular system was investigated for the determination of how much matter must be added to significantly change composite properties. It was determined that polymer chains surprisingly feel the surface of relatively large nanoparticles and pores and that only a very small amount of particles must be added to specific cellulose ester fluids in order to induce gelation.

REFERENCES

[1] S. T. Peters, editor. *Handbook of Composites*. Chapman & Hall, second edition, **1998**.

[2] F. Hussain, M. Hojjati, M. Okamoto, and R. E. Gorga. Polymer-matrix nanocomposites, processing, manufacturing, and application: An overview. *Journal of Composite Materials*, 40(17):1511–1575, **2006**.

[3] Y. Kojima, A. Usuki, M. Kawasumi, A. Okada, Y. Fukushima, T. Kurauchi, and O. Kamigaito. Mechanical properties of nylon 6-clay hybrid. *Journal of Materials Research*, 8(5):1185–1189, **1992**.

[4] D. Adame and G. Beall. Direct measurement of the constrained polymer region in polyamide/clay nanocomposites and the implications for gas diffusion. *Applied Clay Science*, 42(3-4):545–552, **2009**.

[5] E.-H. Kim and B.-J. Lee. Size dependency of melting point of crystalline nano particles and nano wires: A thermodynamic modeling. *Metals and Materials International*, 15(4):531–537, **2009**.

[6] S. Y. Yeo and S. H. Jeong. Preparation and characterization of polypropylene/silver nanocomposite fibers. *Polymer International*, 52(7):1053–1057, **2003**.

[7] J. Zhou, S. Liu, J. Qi, and L. Zhang. Structure and properties of composite films prepared from cellulose and nanocrystalline titanium dioxide particles. *Journal of Applied Polymer Science*, 101(6):3600–3608, **2006**.

[8] Y. Fukushima and S. Inagaki. Synthesis of an intercalated compound of montmorillonite and 6-polyamide. *Journal of Inclusion Phenomena*, 5(4):473–482, **1987**.

[9] Y. Fukushima, A. Okada, M. Kawasumi, T. Kurauchi, and O. Kamigaito. Swelling behaviour of montmorillonite by poly-6-amide. *Clay Minerals*, 23(1):27–34, **1988**.

[10] A. Caballero, J. Morales, and L. Sanchez. Tin nanoparticles formed in the presence of cellulose fibers exhibit excellent electrochemical performance as anode materials in lithium-ion batteries. *Electrochemical and Solid-State Letters*, 8(9):A464–A466, **2005**.

[11] L. Nicolais and G. Carotenuto. *Metal-Polymer Nanocomposites*. John Wiley & Sons, **2005**.

[12] L. Pranger and R. Tannenbaum. Biobased nanocomposites prepared by in situ polymerization of furfuryl alcohol with cellulose whiskers or montmorillonite clay. *Macromolecules*, 41(22):86828687, **2008**.

[13] J. He, T. Kunitake, and A. Nakao. Facile in situ synthesis of noble metal nanoparticles in porous cellulose fibers. *Chemistry of Materials*, 15(23):4401–4406, **2003**.

[14] K. G. Paul, T. B. Frigo, J. Y. Groman, , and E. V. Groman. Synthesis of ultrasmall superparamagnetic iron oxides using reduced polysaccharides. *Bioconjugate Chemistry*, 15(2):394–401, **2004**.

[15] D. Ruan, Q. Huang, and L. Zhang. Structure and properties of cds/regenerated cellulose nanocomposites. *Macromolecular Materials Engineering*, 290(10):1017–1024, **2005**.

[16] I.-W. Shim, S. Choi, W.-T. Noh, J. Kwon, J. Y. Cho, D.-Y. Chae, and K.-S. Kim. Preparation of iron nanoparticles in cellulose acetate polymer and their reaction chemistry in the polymer. *Bulletin of the Korean Chemical Society*, 22(7):772–774, **2001**.

[17] S. Shukla, S. Seal, R. Vij, , and S. Bandyopadhyay. Effect of hpc and water concentration on the evolution of size, aggregation and crystallization of sol-gel nanozirconia. *Journal of Nanoparticle Research*, 4(6):553–559, **2002**.

[18] P. H. Hess and P. H. Parker. Polymers for stabilization of colloidal cobalt particles. *Journal of Applied Polymer Science*, 10(12):1915–1927, **1966**.

[19] J. R. Thomas. Preparation and magnetic properties of colloidal cobalt particles. *Journal of Applied Physics*, 37(7):2914–2915, **1966**.

[20] C. Griffiths, M. Ohoro, , and T. Smith. The structure, magnetic characterization, and oxidation of colloidal iron dispersions. *Journal of Applied Physics*, 50(11):7108–7115, **1966**.

[21] T. W. Smith and D. Wychick. Colloidal iron dispersions prepared via the polymer-catalyzed decomposition of iron pentacarbonyl. *The Journal of Physical Chemistry*, 84(12):1621–1629, **1980**.

[22] R. Tannenbaum. Metal cluster growth limited by polymer surface interactions. *Current Trends in Polymer Science*, 3:81–98, **1998**.

[23] N. Dan, M. Zubris, and R. Tannenbaum. Effect of polymeric media on the kinetics of nanocluster nucleation and growth. *Macromolecules*, 38(22):9243–9250, **2005**.

[24] K. David, E. H. Tadd, R. Tannenbaum, S. Tikku, and N. Dan. Effect of polymer architecture on metal nanoclusters. *Polymer*, 47(25):8344 – 8349, **2006**.

[25] R. Tannenbaum, M. Zubris, E. P. Goldberg, S. Reich, and N. Dan. Polymer-directed nanocluster synthesis: Control of particle size and morphology. *Macromolecules*, 38(10):4254–4259, **2005**.

[26] E. Tadd, A. Zeno, M. Zubris, N. Dan, and R. Tannenbaum. Adsorption and polymer film formation on metal nanoclusters. *Macromolecules*, 36(17):6497–6502, **2003**.

[27] F. M. Winnik, A. Morneau, R. F. Ziolo, H. D. H. Stöver, and W. Li. Template-controlled synthesis of superparamagnetic goethite within macroporous polymeric microspheres. *Langmuir*, 11(10):3660–3666, **1995**.

[28] K. Schölzel. Method of applying a ferromagnetic surface to a base utilizing iron carbonyl and oxygen. U.S. Patent, number 2,919,207, **1959**.

[29] D. Voet and J. G. Voet. *Biochemistry*. John Wiley & Sons, Inc., third edition, **2004**.

[30] E. Ott, H. M. Spurlin, and M. W. Grafflin, editors. *Cellulose and Cellulose Derivatives*. Interscience Publishers, **1954**.

[31] D. A. Rees. *The Shapes of Molecules; Carbohydrate Polymers*. Oliver & Boyd, **1967**.

[32] A. C. O'Sullivan. Cellulose: the structure slowly unravels. *Cellulose*, 4(3):173–207, **1997**.

[33] J. Balfour-Paul. *The Shapes of Molecules: Carbohydrate Polymers*. Fitzroy Dearborn, **1998**.

[34] J. F. Kennedy, G. O. Phillips, D. J. Wedlock, , and P. A. Williams, editors. *Cellulose and Its Derivatives*. Ellis Horwood Limited, **1985**.

[35] P. Rustemeyer. History of ca and evolution of the markets. *Macromolecular Symposia*, 208(1):1–6, **2004**.

[36] M. D. Nicholson. *Reactions of cellulose in the dimethyl sulfoxide/paraformaldehyde solvent*. Ph.D. thesis, Lawrence University, Appleton, WI, **1976**.

[37] J. M. Felix and P. Gatenholm. The nature of adhesion in composites of modified cellulose fibers and polypropylene. *Journal of Applied Polymer Science*, 42(3):609–620, **1990**.

[38] H. Ye, H. Lam, N. Titchenal, Y. Gogotsi, and F. Ko. Reinforcement and rupture behavior of carbon nanotubes-polymer nanofibers. *Applied Physics Letters*, 85(10):1775–1777, **2004**.

[39] S.-L. Gao, E. Mäder, and R. Plonka. Nanocomposite coatings for healing surface defects of glass fibers and improving interfacial adhesion. *Composites Science and Technology*, 68(14):2892–2901, **2007**.

[40] E. Hershkovits, A. Tannenbaum, and R. Tannenbaum. Polymer adsorption on curved surfaces: A geometric approach. *The Journal of Physical Chemistry C*, 111(33):12369–12375, **2007**.

[41] E. Hershkovits, A. Tannenbaum, and R. Tannenbaum. Scaling aspects of block co-polymer adsorption on curved surfaces from nonselective solvents. *The Journal of Physical Chemistry B*, 112(17):5317–5326, **2008**.

[42] E. Hershkovits, A. Tannenbaum, and R. Tannenbaum. Adsorption of block copolymers from selective solvents on curved surfaces. *Macromolecules*, 41(9):3190–3198, **2008**.

[43] S. Wernick, R. Pinner, and P. Sheasby. *The Surface Treatment and Finishing of Aluminum and its Alloys*. ASM International, 5th edition, **1987**.

[44] V. F. Henley. *Anodic Oxidation of Aluminium and its Alloys*. Pergamon Press, **1982**.

[45] A. W. Brace and P. G. Sheasby. *The Technology of Anodizing Aluminum*. Technicopy Ltd., **1979**.

[46] J. C. Scully, editor. *Treatise on Materials Science and Technology*, volume 23. Academic Press, **1983**.

[47] J. O. Bockris, R. E. White, and B. E. Conway, editors. *Modern Aspects of Electrochemistry*, volume 20. Plenum Press, **1989**.

[48] D. A. Jones. *Principles and Prevention of Corrosion*. Prentice Hall, 2nd edition, **1996**.

[49] F. Keller, M. S. Hunter, and D. L. Robinson. Structural features of oxide coatings on aluminum. *Journal of the Electrochemical Society*, 100(9):411–419, **1953**.

[50] J. Brandrup, E. H. Immergut, E. A. Grulke, A. Abe, and D. R. Bloch, editors. *Polymer Handbook*. John Wiley & Sons, 4th edition, **1999**.

[51] J. S. Reed. *Principles of Ceramics Processing*. John Wiley & Sons, Inc., second edition, **1995**.

[52] C. M. Wijmans and E. B. Zhulina. Polymer brushes at curved surfaces. *Macromolecules*, 26(26):7214–7224, **2005**.

[53] D. I. Gittins and F. Caruso. Tailoring the polyelectrolyte coating of metal nanoparticles. *Journal of Physical Chemistry B*, 105(29):6846–6852, **2001**.

[54] I. Piirma and S.-R. Chen. Adsorption of ionic surfactants on latex particles. *Journal of Colloid and Interface Science*, 74(1):90 – 102, **1980**.

[55] J. F. Lawrence. *Organic Trace Analysis by Liquid Chromatography*. Academic Press, **1981**.

[56] C. S. Wu, editor. *Handbook of Size Exculsion Chromatography*, volume 69, pages 25–46. Marcel Dekker, **1995**.

[57] T. Kremer and L. Boross. *Gel Chromatography*. John Wiley & Sons, **1979**.

[58] P. L. Dubin, editor. *Aqueous Size-Exclusion Chromatography*, volume 40, pages 157–170. Elsevier, **1988**.

[59] E. M. Sevick and D. R. M. Williams. Polymer brushes as pressure-sensitive automated microvalves. *Macromolecules*, 27(19):5285–5290, **1994**.

[60] E. M. Sevick and D. R. M. Williams. *MRS Symposium Proceedings: Advances in Porous Materials*, volume 371. MRS, **1995**.

[61] R. Tannenbaum, C. Hakanson, A. Zeno, and M. Tirrell. Spectroscopic study of the chemistry at the cr-pmma interface. *The Journal of Physical Chemistry C*, 18(14):5592–5599, **2002**.

[62] K. Konstadinidis, B. Thakkar, A. Chakraborty, L. W. Potts, R. Tannenbaum, M. Tirrell, and J. F. Evans. Segment level chemistry and chain conformation in the reactive adsorption of poly(methyl methacrylate) on aluminum oxide surfaces. *Langmuir*, 8(5):1307–1317, **1992**.

[63] S. King, K. Hyunh, and R. Tannenbaum. Kinetics of nucleation, growth, and stabilization of cobalt oxide nanoclusters. *The Journal of Physical Chemistry B*, 107(44):12097–12104, **2003**.

[64] R. Tannenbaum, S. King, J. Lecy, M. Tirrell, and L. Potts. Infrared study of the kinetics and mechanism of adsorption of acrylic polymers on alumina surfaces. *Langmuir*, 20(11):4507–4514, **2004**.

[65] R. Hariharan and W. B. Russel. Enhanced colloidal stabilization via adsorption of diblock copolymer from a nonselective solvent. *Langmuir*, 14(25):7104–7111, **1998**.

[66] Y. S. Lipatov and L. M. Sergeeva. *Adsorption of Polymers*. Keter Publishing House, **1974**.

[67] M. Rubinstein and R. H. Colby. *Polymer Physics*. Oxford University Press, **2003**.

[68] Y. S. Lipatov. *Polymer Reinforcement*. ChemTec Publishing, **1995**.

[69] S. S. Zumdahl. *Chemistry*. Houghton Mifflin Co., **1997**.

[70] J. A. Baker, R. A. Pearson, and J. C. Berg. Influence of particle curvature on polymer adsorption layer thickness. *Langmuir*, 5(2):339–342, **1989**.

[71] G. Nunnery, E. Hershkovits, A. Tannenbaum, and R. Tannenbaum. Adsorption of poly(methyl methacrylate) on concave al2o3 surfaces in nanoporous membranes. *Langmuir*, 25(16):9157–9163, **2009**.

[72] M. Aubouy and E. Rapha el. Scaling description of a colloidal particle clothed with polymers. *Macromolecules*, 31(13):4357–4363, **1998**.

[73] M. Aubouy, O. Guiselin, and E. Rapha el. Scaling description of polymer interfaces: Flat layers. *Macromolecules*, 29(22):7261–7268, **1998**.

[74] P. G. de Gennes. Polymer solutions near an interface. adsorption and depletion layers. *Macromolecules*, 14(6):1637–1644, **1981**.

[75] Y. Matsushita, Y. Nakao, K. Shimizu, I. Noda, and M. Nagasawa. Conformations of diblock copolymers in dilute solutions. *Macromolecules*, 21(9):2790–2793, **1988**.

[76] A. Dondos and D. Papanagopoulous. Three models for chain conformation of block copolymers in a solution and in solid state. *Journal of Polymer Science Part B: Polymer Physics*, 34(7):1281–1288, **1996**.

[77] C. Tsitsilianis, G. Staikos, A. Dondos, P. Lutz, and P. Rempp. 1.influence of annealing and casting solvent in the morphology of poly(ethylene oxide)-b-polystyrene-b-poly(ehtylene oxide) triblock copolymers, compatibility effects. *Polymer*, 33(16):3369–3374, **1992**.

[78] V. Subramanian, P. S. Asirvatham, R. Balakrishnan, and T. Ramasami. Molecular mechanics studies on polypropylene and polymethylmethacrylate polymers. *Chemical Physics Letters*, 342(5-6):603 – 609, **2001**.

[79] C. Han and B. Mozer. Conformation of ps-pmma diblock copolymer in toluene by small angle neutron scattering. *Macromolecules*, 10(1):44–51, **1992**.

[80] P. G. de Gennes. Polymers at an interface; a simplified view. *Advances in Colloid and Interface Science*, 27(3-4):189–209, **1987**.

[81] C. Marques, J. F. Joanny, and L. Leibler. Adsorption of block copolymers in selective solvents. *Macromolecules*, 21(4):1051–1059, **1988**.

[82] C. Marques and J. F. Joanny. Block copolymer adsorption in a nonselective solvent. *Macromolecules*, 22(3):1454–1458, **1989**.

[83] J. Bicerano. *Prediction of Polymer Properties*. Marcel Dekker, third edition, **2002**.

[84] C. M. Hansen. *Hansen solubility parameters: a user's handbook*. CRC Press, second edition, **2007**.

[85] O. Karal-Yilmaz, E. E. Gürel, N. Kayaman-Apohan, B. M. Baysal, and F. E. Karasz". Dynamic light scattering studies of poly(methyl methacrylate)polystyrene copolymers in their theta solvents. *Polymer*, 42(23):9433–9440, **2001**.

[86] J. V. Koleske, editor. *Paint and Coating Testing Manual*. ASTM International, 14th edition, **1995**.

[87] J. H. Rolker and T. C. Glasner. Modification of acrylate polymers by treatment with metal carbonyl. U.S. Patent, number 3,959,231, **1973**.

[88] J. H. Rolker and T. C. Glasner. Method of modifying polymers and novel product. U.S. Patent, number 3,959,231, **1976**.

[89] W. G. Fateley and E. R. Lippincott. Normal co-ordinate analysis of the vibrational spectrum of iron pentacarbonyl. *Spectrochimica Acta*, 10(1):8–16, **1957**.

[90] M. F. O'Dwyer. Infrared spectra and normal coordinate analysis of iron pentacarbonyl. *Journal of Molecular Spectroscopy*, 2(1-6):144 – 151, **1958**.

[91] W. F. Edgell, W. E. Wilson, and R. Summitt. The infrared spectrum and vibrational assignment for $Fe(CO)_5$. bonding considerations. *Spectrochimica Acta*, 19(6):863–872, **1963**.

[92] W. F. Edgell and M. P. Dunkle. Some aspects of the infrared spectrum of liquid iron pentacarbonyl and its n-heptane solutions. *Journal of Physical Chemistry*, 68(3):452–456, **1964**.

[93] S. Sato and T. Suzuki. Infrared reflection absorption spectra of $Fe(CO)_5$ adsorbed on au surfaces. *Journal of Electron Spectroscopy and Related Phenomena*, 83(1):85–91, **1997**.

[94] C. Hauchard, C. Pépin, and P. Rowntree. $Fe(CO)_5$ thin films adsorbed on au(111) and on self-assembled organic monolayers: I. structure. *Langmuir*, 21(20):9154–9165, **2005**.

[95] J.-Y. Lee, B.-C. Kang, D.-Y. Jung, and J.-H. Boo. Selective growth of iron oxide thin films using the combined method of metal-organic chemical vapor deposition and microcontact printing. *The Journal of Vacuum Science and Technology B*, 25(4):1516–1519, **2007**.

[96] I. Morjan, R. Alexandrescu, I. Soare, F. Dumitrache, I. Sandu, I. Voicu, A. Crunteanu, E. Vasile, V. Ciupina, and S. Martelli. Nanoscale powders of different iron oxide phases prepared by continuous laser irradiation of iron pentacarbonyl-containing gas precursors. *Materials Science and Engineering: C*, 23(1-2):211 – 216, **2003**.

[97] D. N.-S. Hon and N. Shiraishi, editors. *Wood and Cellulosic Chemistry*. Marcel Dekker, **1991**.

[98] H. Ito, A. B. Padias, and H. K. Hall. Thermal deesterification and decarboxylation of alternating copolymers of styrene with β-substituted t-butyl α-cyanoacrylates. *Journal of Polymer Science Part A: Polymer Chemistry*, 27(9):2871–2881, **1989**.

[99] J. D. Ferry. *Viscoelastic Properties of Polymers*. John Wiley & Sons, Inc., **1961**.

[100] H. H. Winter and F. Chambon. Analysis of linear viscoelasticity of a crosslinking polymer at the gel point. *Journal of Rheology*, 30(2):367–382, **1986**.

[101] T. A. Seder, A. J. Ouderkirk, and E. Weitz. The wavelength dependence of excimer laser photolysis of $Fe(CO)_5$ in the gas phase. transient infrared spectroscopy and kinetics of the Fe(CO)x (x=4,3,2) photofragments. *The Journal of Chemical Physics*, 85(4):1977–1986, **1986**.

[102] P. C. Engelking and W. C. Lineberger. Laser photoelectron spectrometry of the negative ions of iron and iron carbonyls. electron affinity determination for the series Fe(CO)n, n = 0,1,2,3,4. *Journal of the American Chemical Society*, 101(19):5569–5573, **1979**.

[103] K. E. Lewis, D. M. Golden, and G. P. Smith. Organometallic bond dissociation energies: laser pyrolysis of iron pentacarbonyl, chromium hexacarbonyl, molybdenum hexacarbonyl, and tungsten hexacarbonyl. *Journal of the American Chemical Society*, 106(14):3905–3912, **1984**.

[104] E. Weitz. Studies of coordinatively unsaturated metal carbonyls in the gas phase by transient infrared spectroscopy. *The Journal of Physical Chemistry*, 91(15):3945–3953, **1987**.

[105] M. Zubris, R. B. King, and R. Tannenbaum. Kinetics of fe-co nanoalloy formation via decomposition of their carbonyl precursors. *J. Mater. Chem.*, 15(12):1277–1285, **2005**.

[106] J. A. Welch, K. S. Peters, and V. Vaida. Medium effects on the photodissociation of hexacarbonylchromium ($Cr(CO)_6$). *The Journal of Physical Chemistry*, 86(11):1941–1947, **1982**.

[107] H. Khalil, D. Mahajan, M. Rafailovich, M. Gelfer, and K. Pandya. Synthesis of zerovalent nanophase metal particles stabilized with poly(ethylene glycol). *Langmuir*, 20(16):6896–6903, **2004**.

[108] G. Kataby, A. Ulman, R. Prozorov, and A. Gedanken. Coating of amorphous iron nanoparticles by long-chain alcohols. *Langmuir*, 14(7):1512–1515, **1998**.

[109] A. Brenner and R. L. Burwell. The surface chemistry of molybdenum in states of lower oxidation on alumina. *Journal of Catalysis*, 52(3):353–363, **1978**.

[110] A. Brenner and D. A. Hucul. Catalysts of supported iron derived from molecular complexes containing one, two, and three iron atoms. *Inorganic Chemistry*, 18(10):28362840, **1979**.

[111] R. Bjorklund and R. Burwell. The reaction of nickel tetracarbonyl with γ-alumina. *Journal of Colloid and Interface Science*, 70(2):383–391, **1979**.

[112] A. Brenner and D. A. Hucul. The synthesis and nature of heterogeneous catalysts of low-valent tungsten supported on alumina. *Journal of Catalysis*, 61(1):216–222, **1980**.

[113] R. Psaro and S. Recchia. Supported metals derived from organometallics. *Catalysis Today*, 41(1-3):139–147, **1998**.

[114] Y. Kurokawa, H. Ohta, M. Okubo, and M. Takahashi. Formation and use in enzyme immobilization of cellulose acetate-metal alkoxide gels. *Carbohydrate Polymers*, 23(1):1–4, **1994**.

[115] K. Nakane, N. Ogata, and Y. Kurokawa. Formation of inorganic (tac, tan) fibers by thermal decomposition of cellulose acetatetantalum alkoxide precursor gel fibers. *Journal of Applied Polymer Science*, 100(6):4320–4324, **2006**.

[116] F. He, D. Zhao, J. Liu, and C. B. Roberts. Stabilization of fe-pd nanoparticles with sodium carboxymethyl cellulose for enhanced transport and dechlorination of trichloroethylene in soil and groundwater. *Industrial & Engineering Chemistry Research*, 46(1):29–34, **2007**.

[117] K. Buser and W. Heidinger. Hardening of epoxy resins. German patent, number 1054705, **1959**.

[118] M. Pourbaix. *Atlas of Electrochemical Equilibria in Aqueous Solutions*. National Association of Corrosion Engineers, **1974**.

[119] H. Kawanishi, Y. Tsunashima, S. Okada, and F. Horii. Change in chain stiffness in viscometric and ultracentrifugal fields: cellulose diacetate in n,n-dimethylacetamide dilute solution. *Journal of Chemical Physics*, 108(14):6014–6025, **1998**.

[120] H. Kawanishi, Y. Tsunashima, and F. Horii. Dynamic light scattering study of structural changes of cellulose diacetate in solution under couette flow. *Macromolecules*, 33(6):2092–2097, **2000**.

[121] J. E. Kilduff, T. Karanfil, and W. J. Weber. Competitive interactions among components of humic acids in granular activated carbon adsorption systems: Effects of solution chemistry. *Environmental Science & Technology*, 30(4):1344–1351, **1996**.

[122] A. Eftekhari. *Nanostructured Materials in Electrochemistry*. Wiley, **2008**.

[123] R. B. Wehrspohn, editor. *Ordered Porous Nanostructures and Applications*. Springer, **2005**.

[124] G. Hass. On the preparation of hard oxide films with precisely controlled thickness on evaporated aluminum mirrors. *Journal of the Optical Society of America*, 39(7):532–539, **1949**.

[125] J. P. O'Sullivan and G. C. Wood. The morphology and mechanism of formation of porous anodic films on aluminium. *Proceedings of the Royal Society of London Series A: Mathematical and Physical Sciences*, 317(1531):511–543, **1970**.

[126] K. Nielsch, J. Choi, K. Schwirn, R. B. Wehrspohn, and U. G osele. Self-ordering regimes of porous alumina: The 10 porosity rule. *Nano Letters*, 2(7):677–680, **2002**.

[127] G. D. Sulka and K. G. Parkola. Temperature influence on well-ordered nanopore structures grown by anodization of aluminium in sulphuric acid. *Electrochimica Acta*, 52(5):1880–1888, **2008**.

[128] T. T. Xu, R. D. Piner, and R. S. Ruoff. An improved method to strip aluminum from porous anodic alumina films. *Langmuir*, 19(4):1443–1445, **2003**.

[129] L. E. Brus. Electron-electron and electron-hole interactions in small semiconductor crystallites: The size dependence of the lowest excited electronic state. *Journal of Chemical Physics*, 80(9):4403–4409, **1984**.

[130] M. Zhao, X. H. Zhou, and Q. Jiang. Comparison of different models for melting point change of metallic nanocrystals. *Journal of Materials Research*, 16(11):3304–3308, **2001**.

[131] K. Brookes. What's in a name? nano experts seek definitions. *Metal Powder Report*, 61(11):24 – 26, **2006**.

[132] P. Goodhew. Education moves to a new scale. *Nano Today*, 1(2):40 – 43, **2006**.

[133] M. P. Krekeler. Transmission electron microscopy (tem) investigations of mn-oxide rich cathodic material from spent disposable alkaline batteries. *Waste Management*, 28(11):2061 – 2069, **2008**.

[134] M. Sastry, V. Patil, K. Mayya, D. Paranjape, P. Singh, and S. Sainkar. Organization of polymer-capped platinum colloidal particles at the airwater interface. *Thin Solid Films*, 324(1-2):239–244, **1998**.

[135] S. Brunaure, P. H. Emmett, and E. Teller. Adsorption of gases in multimolecular layers. *Journal of the American Chemical Society*, 60(2):309–319, **1938**.

[136] M. J. Hostetler, J. E. Wingate, C.-J. Zhong, J. E. Harris, R. W. Vachet, M. R. Clark, J. D. Londono, S. J. Green, J. J. Stokes, G. D. Wignall, G. L. Glish, M. D. Porter, N. D. Evans, and R. W. Murray. Alkanethiolate gold cluster molecules with core diameters from 1.5 to 5.2 nm: Core and monolayer properties as a function of core size. *Langmuir*, 14(1):17–30, **1998**.

[137] X.-M. Li, J. Huskens, and D. N. Reinhoudt. Reactive self-assembled monolayers on flat and nanoparticle surfaces, and their application in soft and scanning probe lithographic nanofabrication technologies. *Journal of Materials Chemistry*, 14(20):2954–2971, **2004**.

[138] G. Galgali, C. Ramesh, and A. Lele. A rheological study on the kinetics of hybrid formation in polypropylene nanocomposites. *Macromolecules*, 34(4):852–858, **2001**.

[139] D. Marchant and K. Jayaraman. Strategies for optimizing polypropylene-clay nanocomposite structure. *Industrial & Engineering Chemistry Research*, 41(25):6402–6408, **2002**.

[140] R. Krishnamoorti, R. A. Vaia, and E. P. Giannelis. Structure and dynamics of polymer-layered silicate nanocomposites. *Chemistry of Materials*, 8(8):1728–1734, **1996**.

[141] J. D. Sherwood. Cell models for suspension viscosity. *Chemical Engineering Science*, 61(20):6727–6731, **2006**.

[142] C. L. Wu, M. Q. Zhang, M. Z. Rong, and K. Friedrich. Tensile performance improvement of low nanoparticles filled-polypropylene composites. *Composites Science and Technology*, 62(10-11):1327–1340, **2002**.

[143] J. Jancar, A. T. Dibenedetto, and A. Dianselmo. Effect of adhesion on the fracture toughness of calcium carbonate-filled polypropylene. *Polymer Engineering and Science*, 33(9):559–563, **1993**.

[144] Z. Bartczak, A. S. Argon, R. E. Cohen, and M. Weinberg. Toughness mechanism in semicrystalline polymer blends: Ii. high-density polyethylene toughened with calcium carbonate filler particles. *Polymer*, 40(9):2347–2365, **1999**.

VITA

Grady A. Nunnery was born in Rock Hill, SC into a loving family. He is a graduate of Northwestern High School in Rock Hill, SC and Clemson University in Clemson, SC. Hs the author or coauthor of ten technical articles and presentations, as well as several chain letters. He lives in Atlanta with his wife, whom he loves a lot.